Assessing Eolian Snow Redistribution in Din-Gad Catchment, Central Himalaya, using Remote Sensing and Modelling

L.R. van Dijk

In partial fulfilment of the degree of Master of Science

Department of Physical Geography
Utrecht University

April 25, 2023

Supervisors:
Dr. F.M. Nick
Dr. P.D.A. Kraaijenbrink
Prof. Dr. W.W. Immerzeel

Student number	5846668
Discipline	Earth Sciences
Study program	Earth Surface and Water
Specialisation	Geohazards and Earth Observation

Abstract

The Himalaya are amongst the world's most important water towers, supplying water to hundreds of millions of people. They are also vulnerable to climate change, stimulating research on their hydrological behaviour. One important aspect of the hydrological system that is often overlooked in these studies is the eolian redistribution of snow. This study aims to identify eolian snow redistribution patterns using an unprecedented combination of optical remote sensing, downscaled wind fields, a Temperature Index (TI)-based hydrological model (SPHY) and a novel Snow Redistribution mechanism Classification Model (SRCM). This method was applied to Din-Gad Catchment in the Central Himalaya for the period 2017-2020. The results show that eolian snow redistribution patterns are strongly related to the prevailing wind directions and topographic exposure. The most frequent wind-induced snow removal typically occurs in concentrated areas that are exposed in the wind direction, whereas areas of frequent wind-supplied snow deposition are more widespread and located in sheltered areas like valleys and the lee sides of ridges. The wind speed threshold for snow transport is low during the winter months and increases in the monsoon season, due to the increasing age and wetness of the snowpack in that period. SRCM classified 21.6% of snow cover changes as wind-driven and 14.1% as gravity-driven. The classified snow redistribution mechanisms were evaluated using satellite images, finding that SPHY had difficulty classifying observed snow cover changes with the chosen model parameters. This indicates that modelling snow cover change using only temperature and precipitation data is an oversimplification and that wind-induced snow dynamics play a significant role in the spatiotemporal distribution of snow cover in Din-Gad Catchment. This also suggests that TI-based hydrological models like SPHY would benefit from the incorporation of snow redistribution processes. Recommendations for improving these methods include using radar imagery, incorporating field observations and performing sensitivity analyses and error propagation tests. This study contributes to understanding the role of snow redistribution in high-mountain areas, which is critical for designing accurate models that can make reliable predictions of hydrological behaviour.

Keywords: hydrology, snow dynamics, snow redistribution, wind fields, remote sensing, modelling.

Contents

6 Conclusion   40

Acknowledgements   41

Data availability   41

References   42

1   Introduction

1.1   The Himalayan water towers and climate change

Mountains supply large parts of the world's water demands, both natural and anthropogenic (Immerzeel et al., 2010; Viviroli et al., 2007). This makes them the world's water towers. According to their water supply and downstream dependence, the world's most important water towers are also the most vulnerable to climatic and socio-economic changes (Immerzeel et al., 2020). Amongst the most important are the Himalaya. This mountain range is the source of several major river systems that provide hundreds of millions of people with a freshwater supply that is used for consumption, irrigation and hydroelectric power generation (Biemans et al., 2019; Immerzeel et al., 2020; Immerzeel et al., 2010; Viviroli et al., 2007). Their downstream regions are densely populated and intensively irrigated (Immerzeel & Bierkens, 2012; Lutz et al., 2014a).

Climate change imposes significant changes in the hydrological system of the Himalayas, implying severe consequences for the water availability in this region (Khanal et al., 2021). An assessment of the current-century climate change impact on the hydrology of high-mountain Asia has shown that the responses vary depending on the hydrological regime and time scale, but show a general pattern. At the seasonal scale, melting and its associated water availability will shift to earlier in the year (Khanal et al., 2021). At the decadal scale, the magnitude of melting and water availability will increase and at the century scale, it will decrease.

The impact of climate change on glaciers in high-mountain Asia has been extensively studied because of their contribution to water supply (Biemans et al., 2019; Immerzeel et al., 2010; Nie et al., 2021) and the predicted future changes therein (Huss & Hock, 2018; Kraaijenbrink et al., 2017; Rounce et al., 2020). The role of snow has also been researched at the regional scale (Armstrong et al., 2019; Biemans et al., 2019; Immerzeel et al., 2010; Kapnick et al., 2014; Kraaijenbrink et al., 2021). Snowmelt contributes more to runoff than glacier melt does and future snowmelt runoff may decrease considerably (Kraaijenbrink et al., 2021). The contribution of snowmelt to runoff will continue to decrease under every future climate scenario, but the magnitude of the decrease depends on the degree of warming, drying or wetting. Despite the difficulties in quantifying Snow Water Equivalent (SWE) using remote sensing (Bormann et al., 2018; Dozier et al., 2016; Smith & Bookhagen, 2018, 2020), understanding the role of snow in the region's hydrological system is essential to unravel the environmental processes that occur in high-mountain Asia (Huss et al., 2017; Livneh & Badger, 2020; Qin et al., 2020).

1.2   The role of snow in the hydrological system

A study on snow resource potential for human water demand in the present and future found that 77-105% of the unmet water demand in large Himalayan basins is supplied by snowmelt runoff (Mankin et al., 2015). Under future climate scenarios, snow resource potential has a 33-63% risk of decreasing in

these snow-sensitive basins, leading to a decline in the buffering capacity of snow for water availability. This will affect over 966 million people living in the Indus and Ganges river basins. Also, snowmelt and snowpack duration influence the volumetric and temporal characteristics of water availability within catchments (Barnett et al., 2005; Beniston & Stoffel, 2014). This illustrates the importance of snow cover in the hydrological system.

Due to constraints on data availability, snow is often modelled using a Temperature Index (TI) approach (Armstrong et al., 2019; Hock, 2003; Khanal et al., 2021; Khanal et al., In Review; Kraaijenbrink et al., 2021). Such an approach omits potentially important snow dynamics that contribute to SWE changes, such as sublimation and redistribution, and thus lacks an accurate representation of snow ablation processes. This is important because climate change will affect the prevailing wind patterns (Lobeto et al., 2022), resulting in changing snow redistribution and associated water storage. A thorough understanding of snow dynamics is required to make reliable water availability predictions and to support effective future water resource management.

Snow redistribution may take place due to wind or gravity. Wind-induced (eolian) snow transport can alter the existing snow cover significantly (Balk & Elder, 2000; Bernhardt et al., 2009; Bowling et al., 2004; Mott & Lehning, 2010; Pomeroy et al., 1998). Snow is generally transported from windward to leeward sides of obstacles such as mountain faces or vegetation (Dadic et al., 2010; Hiemstra et al., 2002; Liston & Sturm, 1998; Mott & Lehning, 2010; Pomeroy et al., 1998). This changes the energy balance, spatial SWE patterns, the timing and magnitude of runoff, avalanche risk and sublimation rates (Brauchli et al., 2017; Dadic et al., 2010; Lehning et al., 2006; Liston, 1995; Liston & Sturm, 1998; Strasser et al., 2008; Zhang et al., 2022).

1.3   Studying the redistribution of snow

Numerous models exist that aim to predict the lateral redistribution of snow for hydrological or climate research purposes (Déry & Yau, 1999; Essery et al., 1999; Lehning et al., 2006; Liston, 2004; Liston & Sturm, 1998; Winstral et al., 2002). However, the accuracy of these (mostly physically-based, numerical) models is heavily dependent on the quality of the meteorological input data. Concerning wind-driven snow transport processes, the models are particularly sensitive to wind speed and wind direction parameters (Bernhardt et al., 2009; Dadic et al., 2010; Eidsvik et al., 2004; Essery, 2001; Liston & Sturm, 1998). Over the years, progress has been made in increasing the spatiotemporal resolution of modelling snow dynamics in mountainous areas (Bernhardt et al., 2010a; Bernhardt et al., 2009; Freudiger et al., 2017; Liston & Elder, 2006; Mott & Lehning, 2010).

More recently, the effects of gravitational and eolian snow redistribution on snowmelt and sublimation were studied using a spatially distributed snow-evolution model (Bernhardt et al., 2012). This study was performed in a study area of ca. 200 km^2 with an elevation span of ca. 2000 m in the Northern Alps. The study found reduced melt rates on crests and steep walls and increased snowmelt in glaciated areas and at foothills, due to snow being moved from exposed to sheltered locations. Additionally, the

effects on snowmelt were largest when small scales were considered (i.e. 60 m) and (almost) negligible at scales over 2000 m. However, this study was conducted in an much more topographically gentle area than the Himalaya.

Similar analyses with other models and in other areas could lead to improved understanding of the effects of snow redistribution on the accuracy of hydrological model output variables such as melt (Bernhardt et al., 2012; Freudiger et al., 2017). This is valuable to the future development of hydrological models, which enable projections of future runoff behaviour. Improving the reliability of these projections is paramount to increasing water security, as local authorities depend on these forecasts to design and implement water resource management strategies.

1.4   Research gap and questions

Snow has an important role in the hydrological system of high-mountain Asia. Climate change affects this in multiple ways. In the future, snowmelt contribution to runoff will decrease and the prevailing wind patterns will change, resulting in changing snow behaviour patterns. Snow dynamics have been extensively studied, often using TI-based hydrological models, which do not consider snow redistribution. Previous studies have addressed this by modelling the lateral redistribution of snow and thus providing a more complete representation of snow ablation processes. However, the accuracy of these studies is limited by several factors, including spatiotemporal resolution, quality of meteorological input data and application to similar topographies.

The patterns of eolian snow redistribution in the Himalaya remain to be studied. This research gap can be addressed using a combination of high-resolution satellite imagery, climate reanalysis data and a TI-based hydrological model. The latter has recently been used to model temperature-driven snow processes in the Himalaya (Khanal et al., In Review), providing a reference for snowmelt and snowfall without requiring additional computation.

The main research question of this study is: "What are the patterns of eolian snow redistribution in the Himalaya as can be identified using remote sensing, modelling, climate reanalysis data and reference data from a TI-based hydrological model?" To answer this question, the following sub-questions are defined:

1. To what extent is optical satellite imagery suitable for SC change mapping over complex terrain?
2. How does the snow cover evolve in response to ablation, accumulation and redistribution?
3. To what extent are wind fields from downscaled climate reanalysis data suitable for evaluating eolian snow redistribution patterns?
4. How much snow cover change is overlooked by using a TI-based hydrological model without considering eolian snow redistribution?

Section 2 describes the study area for this research. Section 3 details the methods and techniques used

to conduct this study. The results are presented in Section 4. Interpretations of the results, a discussion of the applications, limitations and implications of this study and recommendations for future research are provided in Section 5. Finally, the conclusions are given in Section 6.

2   Study area

Recently, a study was conducted on the hydrological changes in the Bhagirathi Basin using a TI-based hydrological model (Khanal et al., In Review). This basin is located in the state of Uttarakhand in Northern India. Located within the basin is Din-Gad Catchment, which extends from latitude 30°48' to 30°54' N and longitude 78°39' to 78°52' E. The catchment covers an area of 77.8 km^2 and has strong relief gradients (Figure 1), making it a suitable area for this study. Additionally, the results of the recent study provide reference data for snowfall and snowmelt, which are relevant for identifying temperature-driven snow cover changes (Khanal et al., 2021).
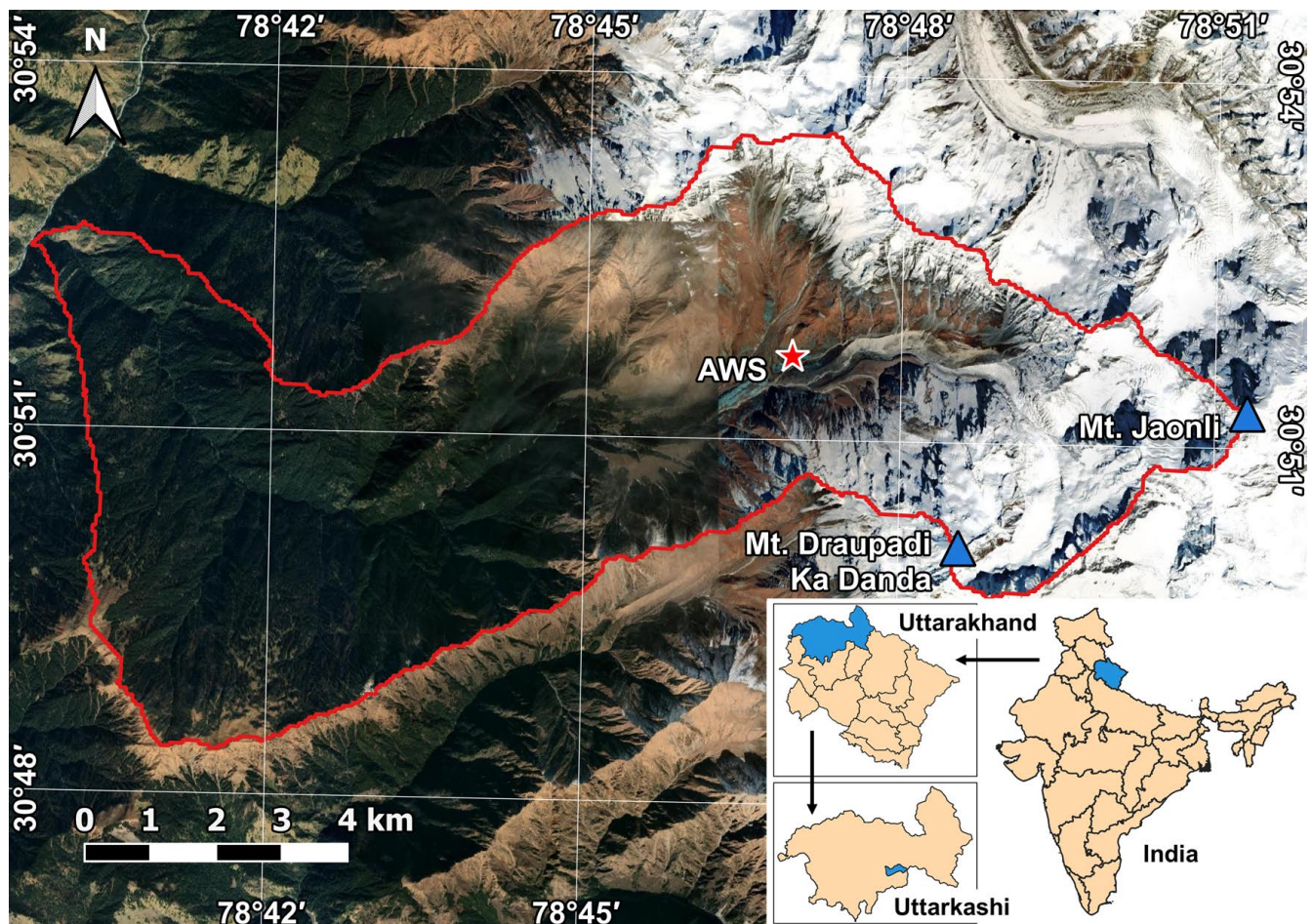
Figure 1: Overview of Din-Gad Catchment. The red line delineates the catchment boundary, the blue triangles indicate noteworthy mountain peaks and the red star indicates the location of an Automatic Weather Station (AWS).

Din-Gad Catchment is home to Dokriani Glacier, which originates between the two highest peaks in the catchment: Mount Jaonli (6578 m a.s.l.) in the east and Mount Draupadi Ka Danda (5716 m a.s.l.)

in the southeast. The glacier flows northwards for 2 km, then turns westwards and flows for another 3 km before reaching its end at 3965 m a.s.l. (Pratap et al., 2015). Dokriani Glacier feeds the Din-Gad tributary, which flows westwards into the Bhagirathi River, an important tributary of the Ganges, at the westernmost point of the catchment (1740 m a.s.l.).

In terms of land cover, there is a gradient from east to west, determined by elevation and thus temperature differences. The easternmost, highest part of the study area is permanently covered with snow and ice. Towards the west and with decreasing elevation, this transitions into barren land, grasslands and evergreen forests. More specifically, herbaceous annuals and evergreen shrubs cover approximately 31% of the catchment and broadleaf and conifer trees can be found with increasing vegetation cover towards the west, covering 54% of the catchment (Buchhorn et al., 2020; Friedl & Sulla-Menashe, 2022; Thayyen et al., 2007).

The climate in the study area is temperate and strongly influenced by topography. Summer temperatures range between freezing and 20°C, averaging around 8°C. In winter, temperatures can drop to -30°C, with an average of around -10°C. From May to October, average precipitation in Din-Gad Catchment amounts to 1000-1600 mm (Thayyen et al., 2007). The monsoon season, which generally lasts from mid-June to mid-September, accounts for 40-50% of this precipitation. Despite the monsoon, yearly precipitation in Din-Gad Catchment is relatively low compared to the Uttarkashi district average, due to its location in the rain shadow of the surrounding Himalaya (Chauhan, 2010).

Many aspects of Din-Gad Catchment have been studied in the past, including glacier mass balance, hydrology and meteorology (Pratap et al., 2015; Thayyen et al., 2007; Yadav et al., 2021). The Bhagirathi basin has also been intensively studied regarding snow cover, meteorology, flood hazards, ecological vulnerability, climatology and hydrology (Dimri et al., 2022; Gourav et al., 2020; Joshi et al., 2015; Rehman et al., 2022a; Rehman et al., 2022b; Rehman et al., 2021; M. K. Singh et al., 2021). Due to its location and elevation, relatively sparse vegetation cover and contribution to the downstream water supply, Din-Gad Catchment is a suitable study area for this research.

3 Methods

High-resolution satellite imagery, climate reanalysis data and a TI-based hydrological model, amongst other resources, provide means for studying eolian snow redistribution patterns. This is yet to be researched in the Himalaya and is relevant to improving hydrological models. The methodology of this study consisted of five main steps: (1) remote sensing of snow cover, (2) obtaining downscaled wind fields and topographic exposure maps, (3) obtaining modelled SC reference data from a TI-based hydrological model, (4) avalanche susceptibility mapping and (5) developing and using a snow redistribution mechanism classification model. Ultimately, the results of the classification model were aggregated to identify eolian snow redistribution patterns and compared to the output of the hydrological model, which does not incorporate snow redistribution processes.

3.1 Remote sensing of snow cover

Snow cover (hereafter 'SC') can be derived from multispectral satellite imagery using remote sensing techniques. For this study, optical imagery was used from three satellite platforms: Sentinel-2, Landsat 8 and PlanetScope. This combination has been shown to perform well for land cover change mapping (Acharki, 2022; Roy et al., 2019). For each platform, the surface reflectance dataset was used so that no atmospheric correction was required. The processing of the imagery was done using Google Earth Engine, a scalable geospatial analysis platform that provides powerful cloud computing capabilities and public access to a large catalog of planetary data sets (Gorelick et al., 2017). The chosen period of interest was January 1, 2017, to December 31, 2020, for two reasons. Firstly, significantly more scenes with a cloud cover <40% were available for the study area from 2017 onwards. Secondly, the snowfall and snowmelt reference data (Khanal et al., In Review) were only available until the end of 2020.

The pre-processing of images consisted of filtering for scenes within the study area and period of interest, removing scenes with a cloud cover $\geq$40%, resampling the Sentinel-2 and PlanetScope imagery to match the resolution of Landsat 8 (30 m), masking remaining clouds, filtering for a maximum of one image per day and clipping to the study domain. The cloud masking was done using the 'cloud high probability' class of the built-in quality assessment bands, which indicate clouds with a probability of >65%. When multiple images were available for a given day, the mean composite was used for that day, giving preference to Sentinel-2 and Landsat 8 images over PlanetScope images. This preference is explained below. After pre-processing, a total of 647 images remained for the 1461 days of interest, resulting in an average of almost one image per two days (Figure 2).
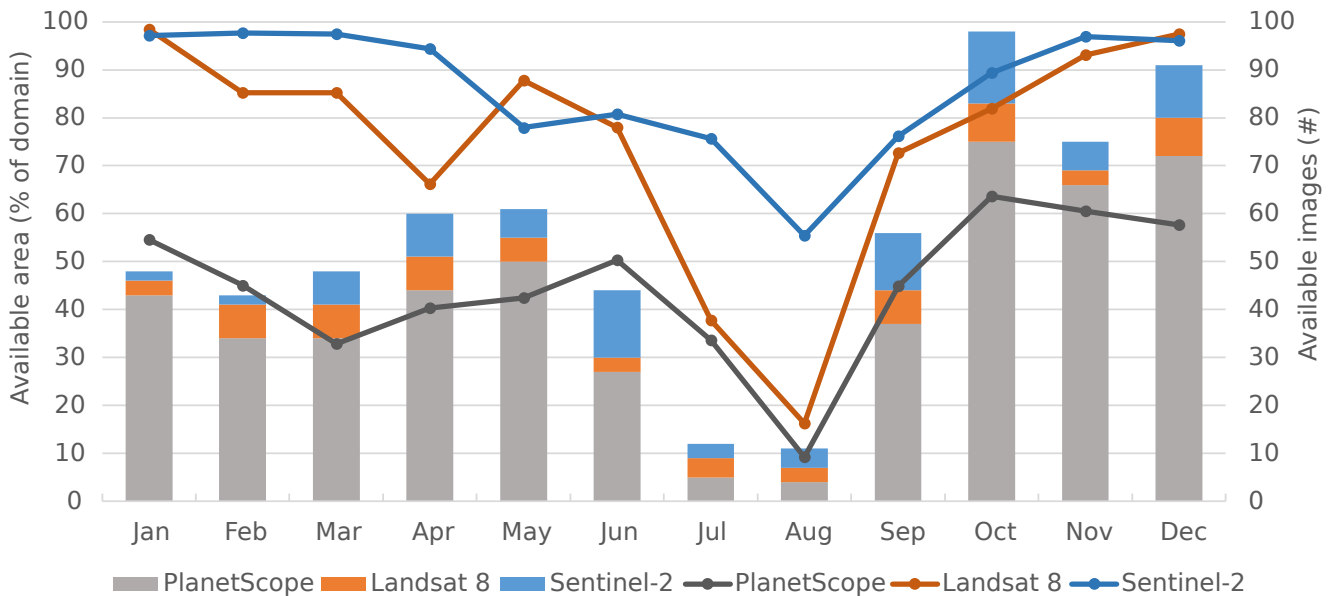
Figure 2: Availability of satellite images per platform and per month. The line shows the mean available area as a percentage of the study domain. The stacked bars show the number of available images. Note that although scenes with $\geq$40% cloud cover were excluded, multiple points show an available area of <60%. This is because the cloud cover for the portion of the scene that intersects the study domain can be lower than the cloud cover for the entire scene.

Snow and clouds are both highly reflective in the visible wavelengths of the electromagnetic spectrum. However, snow absorbs light in the short-wave infrared part of the spectrum, whereas clouds do not. Hence, a short-wave infrared (SWIR) band can be used to distinguish between snow and clouds (Hall & Riggs, 2010). To obtain binary SC maps from optical imagery, the Normalized Difference Snow Index (NDSI) was computed according to Equation 1:

$$\text{NDSI}_{S2} = \frac{\text{Green}_{B3} - \text{SWIR}_{B11}}{\text{Green}_{B3} + \text{SWIR}_{B11}} \quad \text{or} \quad \text{NDSI}_{L8} = \frac{\text{Green}_{B3} - \text{SWIR}_{B6}}{\text{Green}_{B3} + \text{SWIR}_{B6}} \quad (1)$$

where S2 refers to Sentinel-2, L8 refers to Landsat 8 and B refers to the band number. Histograms of NDSI values for both platforms indicated a bimodal distribution with a minimum at NDSI=0.2 for all seasons. Therefore, a constant NDSI threshold of 0.2 was applied to distinguish between snow-covered (NDSI>0.2) and snow-free (NDSI<0.2) pixels, resulting in binary SC maps.

PlanetScope satellites are not equipped with a SWIR sensor, making computation of the NDSI impossible. This gives reason to prefer Sentinel-2 and Landsat 8 images over PlanetScope images when multiple images are available for a given day. However, PlanetScope imagery contains Usable Data Mask 2 (UDM2) bands, in which certain types of surface or atmosphere interference classes are pre-classified based on supervised machine learning techniques ("UDM 2", 2022). The classification model used for this is trained using truth scenes sourced from different satellites, scene contents, seasonalities, geographies and cloud types. UDM2 band 2 provided the binary SC maps for the PlanetScope imagery.

3.2 Wind fields and topographic exposure

High-resolution wind fields are required to study eolian snow redistribution because snow transport occurs above certain wind speeds and its direction is dependent on the wind direction. Additionally, a topographic exposure parameter can be a significant predictor of observed snow distribution when included in spatial snow distribution models (Winstral et al., 2002). Therefore, downscaled wind fields and topographic exposure maps were used for this study.

3.2.1 Downscaling of wind fields using WindNinja

Wind data from Numerical Weather Prediction (NWP) models were considered too coarse-resolution for this study. Therefore, climate reanalysis data were downscaled to obtain high-resolution wind fields. This was done using the WindNinja-3.8.0 application developed by the Missoula Fire Sciences Laboratory of the US Forest Service (Wagenbrenner et al., 2016) and wind speed and direction data from the ERA5-Land product of the European Centre for Medium-Range Weather Forecasts (ECMWF) (Muñoz-Sabater et al., 2021).

The theoretical background of WindNinja is detailed by Forthofer et al. (2014). Here, a brief overview of the model framework is given. WindNinja is a mass-consistent diagnostic wind model used for downscaling wind fields from NWP models. The application employs variational calculus techniques

to obtain numerical solutions, conserving mass both locally and globally, i.e. within each cell and over the entire domain. The model provides two solving algorithms: (1) conservation of mass and (2) conservation of mass and momentum. The mass conservation solver uses the finite element method to minimize change from the initial wind field. The mass-momentum conservation solver uses the finite volume method to account for incompressible turbulent flow. The latter is more computationally intensive but gives more accurate results in regions where momentum effects are important (e.g., on the leeward side of terrain features).

WindNinja requires three main inputs. Firstly, a Digital Elevation Model (DEM) is required, upon which a terrain-following mesh is constructed, consisting of layers of hexahedral cells with variable height, representing the air. Secondly, an initial wind field is required, for which three options are available. The model can be initialized with (1) a user-defined domain-averaged wind field (height, speed and direction), (2) wind measurements from one or more Automatic Weather Stations (AWS) or (3) wind data from an NWP model. Option 2 is currently not available for the mass-momentum conservation solver and option 3 is limited to a list of NWP models that only provide data for North America. Lastly, WindNinja assumes a homogeneous vegetation cover of either grass, brush or trees over the entire domain. This determines the surface roughness and associated drag.

Additional options in WindNinja include diurnal slope winds and non-neutral atmospheric stability. The diurnal slope wind model is designed to compute small-scale slope winds, but not large-scale valley winds or other buoyancy-driven flows such as sea or land breezes. The non-neutral atmospheric stability option accounts for the resistance of the atmosphere to vertical motion by computing surface heat flux and the vertical air density profile. At present, this option can simulate simplified non-neutral flows (i.e. flow around a terrain feature in a stable atmosphere versus flow over a terrain feature in an unstable atmosphere), but not complex phenomena such as wave and breaking-wave structures, severe down-slope winds or thunderstorms. Also, the non-neutral atmospheric stability option is currently unavailable for the mass-momentum conservation solver. However, this is no problem for simulating wind over snow-covered terrain, as this is generally dominated by near-neutral conditions (Cullen et al., 2007).

WindNinja assumes the air to be incompressible and does not account for latent heat effects or conservation of energy. Due to computational limitations, the developers recommend that the model domain is smaller than 50x50 km and that the resolution of the model output is set no finer than 100 m. Larger domains (>2500 km^2) and finer resolutions (<100 m) can lead to unrealistic results. The terrain provided by the DEM is approximated by a finite number of points, leading to the smoothing of terrain features.

To obtain high-resolution wind fields, WindNinja was run for daily time steps (from January 1, 2017, to December 31, 2020) with the mass conservation solver and for a resolution of 100 m. As input DEM, NASA's Shuttle Radar Topography Mission (SRTM) V3, with a spatial resolution of 30 m, was used (Farr et al., 2007). Each time step was initialized with the domain-averaged maximum wind speed and

corresponding wind direction of that day, as derived from ERA5-Land. Diurnal slope winds were not included, as the availability of satellite imagery was insufficient to facilitate analysis at the sub-daily time scale. Atmospheric stability was set to neutral because near-neutral atmospheric conditions usually persist over snow-covered terrain (Cullen et al., 2007). 'Brush' was set as the prevailing vegetation type to provide a balanced estimate for the entire study domain.

The output consisted of one GIS vector layer per day, containing one wind speed (m/s) and direction (degrees) value per 100 m grid cell. To ensure that the wind fields were in the same data format as the SC maps, the output was converted to two-band raster layers and resampled to a 30 m resolution using the nearest neighbour technique.

3.2.2 Topographic exposure

Topographic exposure was computed for all cells in the study domain and for each (inter)cardinal wind direction using a method proposed by Winstral et al. (2002). This method computes topographic exposure of a cell based on the height and distance of the surrounding horizon, in this case, derived from the 30 m SRTM V3 DEM. These two measures determine the angle of inflection from the horizon, which was computed at a cell-by-cell interval (30 m) from a distance of 30 m up to 5000 m for 8 wind directions (N, NE, E, SE, S, SW, W and NW). For each direction, the maximum angle determined the exposure in that direction and the domain mean value indicated the threshold between sheltered and exposed locations. The resulting 8-band topographic exposure image was used in conjunction with the downscaled wind fields to identify locations that are most susceptible to eolian snow redistribution, as explained in Section 3.5.

3.3 Hydrological model: SPHY

To identify snow melt and accumulation, reference data generated by the hydrological model 'SPHY' were used. SPHY (Spatial Processes in HYdrology, Terink et al. (2015)) is a spatially distributed model that simulates hydrological processes on a cell-by-cell basis. The model code is written in Python and based on the PCRaster dynamic modelling framework (Karssenberg et al., 2010). The main processes that are simulated by SPHY include those related to rainfall-runoff, cryosphere, evapotranspiration, dynamic evolution of vegetation cover, lake and reservoir outflow and root-zone moisture contents. The existing snow module of SPHY does not include snow redistribution processes, as it simulates snow cover using temperature and precipitation data only.

The input data used for modelling snow cover evolution with SPHY was sourced from ECMWF's ERA5 product (Hersbach et al., 2020). This has a native spatial resolution of 30 km, which was inadequate for this study. To increase the resolution, the data was downscaled to 50 m using the topography-based downscaling scheme TopoSCALE v.1.0 (Fiddes & Gruber, 2014). TopoSCALE accounts for temporally varying lapse rates by performing a 3D interpolation of atmospheric fields available on the pressure levels of the ERA5 product. Also, TopoSCALE accounts for the main topographic effects on

atmospheric forcing by performing a topographic correction of radiative fluxes based on a high-resolution DEM.

The SPHY model was run for the period 1991-2020 using daily time steps and a spatial resolution of 50 m (Khanal et al., In Review). The relevant input parameters were: a temperature threshold below which precipitation falls as snow (T_{crit}) of 0.7°C, a degree-day factor for snow (DDF_s) of 6.1 mm °C^{-1} day^{-1} and a threshold indicating the minimum snow storage for the ground cover to be considered snow of 5.0 mm. The model was calibrated to better represent observations in the study area by modifying the downscaled ERA5 input data. The precipitation values were multiplied by a factor of 1.52 and the temperature values were increased by 2.5°C to match the observed mass balance and river discharge.

The SPHY output data of interest were daily snow storage maps (in mm) from January 1, 2017, until December 31, 2020. These raster maps were converted to binary SC maps by applying the threshold value of 5.0 mm. The maps were then resampled to a 30 m resolution using the nearest neighbour technique to obtain the same resolution as the satellite-derived SC maps and the wind fields.

3.4   Avalanche susceptibility mapping

Avalanches are an abundant phenomenon in the Himalaya. They are considered to be one of the deadliest natural hazards in the region (A. Singh & Ganju, 2002). Extensive research has been done on the formation of avalanches. Controlling factors include terrain (slope, aspect, curvature, elevation, terrain roughness, ground cover), snow (holding depth, wetness, density, texture), wind and temperature (Schweizer et al., 2003).

A widely used GIS-based decision support system, that can be used as a method for mapping avalanche susceptibility, is a Multi-Criteria Decision Analysis - Analytical Hierarchy Process (MCDA-AHP) model (Jiang & Eastman, 2000; Saaty, 1990). The theoretical background of the AHP model is provided by Nefeslioglu et al. (2013). In short, the MCDA-AHP model solves decision-making problems by hierarchically arranging the problems and assigning an importance or preference rating (on a scale of 1-9) and a relative weight to each decision criterion. The application of this method for avalanche susceptibility mapping in Northwestern India has been demonstrated with an accuracy of 91% (Kumar et al., 2017). The advantage of this method is that avalanche susceptibility can be mapped without snow depth data.

For this purpose, the decision criteria are the factors that control avalanche susceptibility. These are discretized into classes, which each receive a preference rating, where 1 is the lowest preference (i.e. least susceptible to avalanching) and 9 is the highest preference (i.e. most susceptible to avalanching). Relative weights are then assigned to each controlling factor, where the factor that exerts most control receives the highest weight.

Using this method, a previous study was conducted on the Gangotri glacier, which is situated just

outside of Din-Gad Catchment, to the northeast (Snehmani et al., 2014). Through verification of the ASI calculations with ground observations, this study found that avalanches had occurred in 85.82% of the modelled high-susceptibility area. Conversely, 86.39% of the avalanche-affected areas were covered by the high-susceptibility class. As the topography surrounding the Gangotri glacier is very similar to that of Din-Gad Catchment, the results of Snehmani et al. (2014) were considered representative of Din-Gad Catchment. The selected decision criteria, their relative weights and the ratings of the criterion's classes are displayed in Table 1.

Decision criterion	Weight	Class	Preference rating
Aspect	0.1110	N	9
		NE	9
		E	3
		SE	7
		S	3
		SW	1
		W	1
		NW	4
		Flat	1
Curvature	0.1157	< 0 (convex)	9
		0	4
		> 0 (concave)	1
Elevation	0.2428	1700-3800 m	1
		3800-4200 m	2
		4200-4600 m	4
		4600-5000 m	7
		5000-5400 m	9
		5400-5800 m	9
		5800-6200 m	7
		6200-6600 m	3
Ground cover	0.0570	Snow	9
		No snow	1
Slope	0.4735	$< 12°$	1
		12-25°	4
		25-45°	9
		$> 45°$	3

Table 1: Decision criteria and their relative weights, classes and preference ratings for use in an MCDA-AHP model to map avalanche susceptibility (Snehmani et al., 2014). These values were obtained for the Gangotri glacier and used in Equation 2 to compute ASI values for Din-Gad Catchment.

Using the values from Table 1, the SRTM V3 DEM and the satellite-derived SC maps, the dimensionless Avalanche Susceptibility Index (ASI) was calculated for each 30 m grid cell of all 647 images as follows:

$$\text{ASI} = 0.4735S + 0.2428E + 0.1157C + 0.111A + 0.057G \tag{2}$$

where S, E, C, A and G are the preference ratings of slope, elevation, curvature, aspect and ground cover, respectively.

After computing the ASI, the results were categorized into four classes: minimal, low, moderate and high susceptibility. This was done using the Jenks natural breaks optimization method. This method identifies data clusters by iteratively comparing the sum of the squared difference between within-class values and class means (Jenks, 1967). The ability of this classification method to accurately discretize ASI classes has been demonstrated in a study area with similar topography to Din-Gad Catchment (Kumar et al., 2017).

3.5   Snow Redistribution Classification Model (SRCM)

Comparison of SC maps from consecutive images enables the identification of snow redistribution patterns. However, these patterns include all transport mechanisms, whereas mainly the eolian redistribution was of interest for this study. Therefore, a distinction was made between transport mechanisms. Firstly, snowmelt in one location and snowfall in another can be misinterpreted as redistribution. Secondly, snow redistribution can occur due to gravity (avalanching). Lastly, snow redistribution can be driven by wind.

The satellite-derived SC maps were exported from Google Earth Engine to be further analysed using Python 3.7.3. (van Rossum, 2023). The new Snow Redistribution Classification Model (SRCM) was developed to analyse the temporal evolution of snow cover. The model performs an image-by-image comparison of SC maps, identifying areas of snow removal and deposition and classifying the mechanisms responsible for these dynamics. The required input data and the decision criteria used to classify the mechanisms are detailed below and visualized in Figure 3.

3.5.1   SRCM input

SRCM requires multiple datasets as input, both static (i.e. time-independent) and multitemporal. The static inputs include the SRTM V3 DEM, the 8-band topographic exposure image, a rasterized delineation of watersheds and a raster map of the distance of each cell to its watershed outlet. The multitemporal inputs include the downscaled wind fields for all 1461 days of interest, the ASI and SC maps for all 647 satellite images and the SPHY SC maps for the corresponding 647 days.

The watersheds raster was derived from the DEM and used to compute the Euclidean distance of each cell to its watershed outlet. All the required input datasets were georeferenced raster files (coordinate reference system EPSG:32644) consisting of a 638x361 grid of 30x30 m cells covering the study domain.
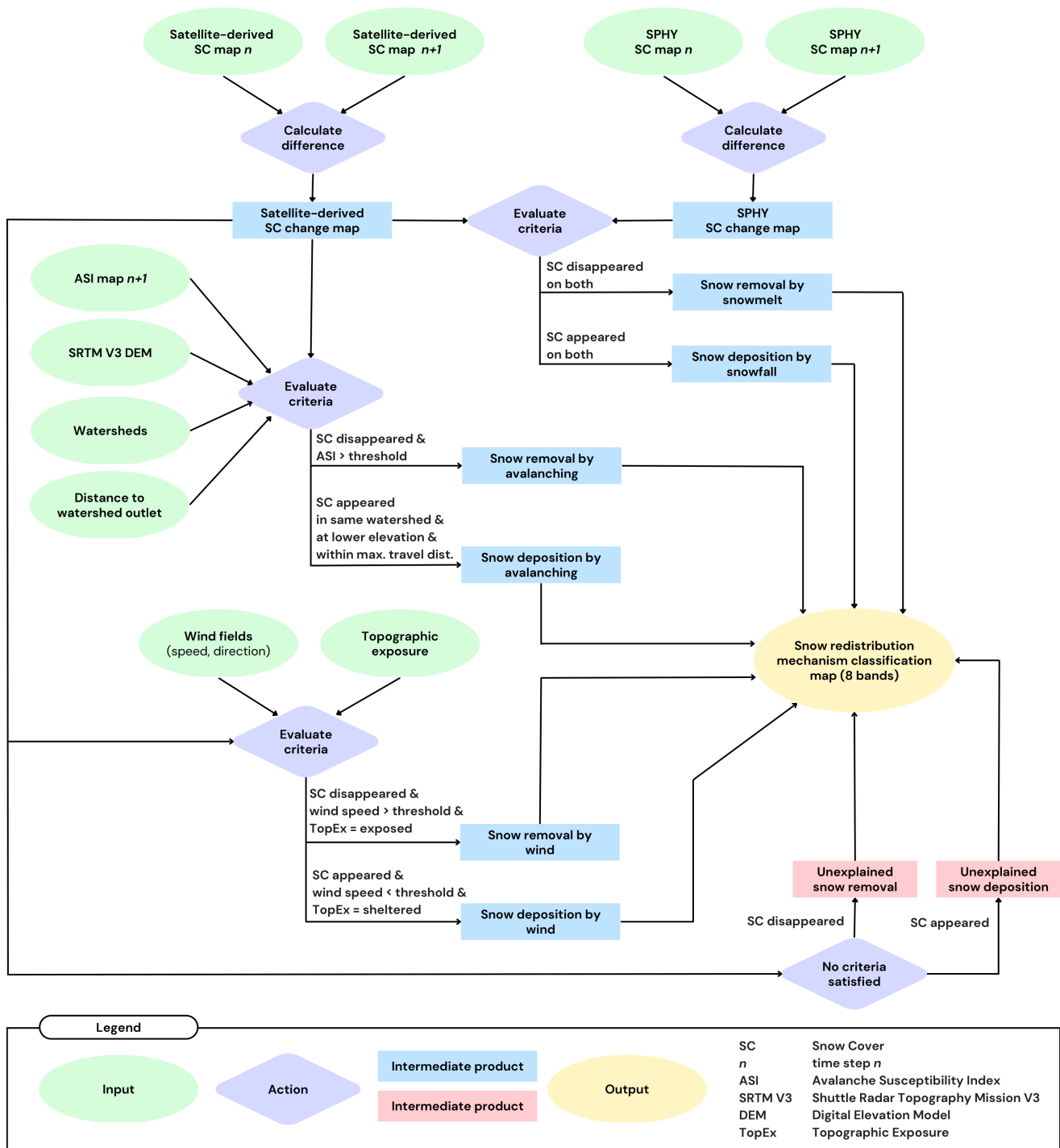
Figure 3: Flowchart of SRCM's classification scheme. Ovals and rectangles depict rasters of 30x30 m cells on a 638x361 cell grid. Diamonds depict actions that are performed cell-by-cell. Arrows indicate the direction of data flow. This scheme is repeated for each pair of subsequent dates.

This enabled cell-by-cell evaluation of snow redistribution mechanisms, as described in the following paragraphs. Additionally, SRCM requires the user to set several parameters. These include the ASI threshold, the maximum travel distance for avalanches and the wind speed threshold for snow transport. The values used for this study are explained below.

3.5.2 Classification of snowfall and snowmelt

SRCM's classification scheme iterated over all 647 dates corresponding to the satellite images. For each pair of subsequent dates, two SC change maps were computed: one from the satellite-derived SC maps and one from the SPHY SC maps. These indicated whether snow cover appeared, disappeared or remained unchanged between the two subsequent dates, according to the satellite images or SPHY. Note that SPHY is a TI-based model, where the only snow deposition and removal mechanisms simulated are snowfall and snowmelt.

To classify cells where snowfall or snowmelt had taken place between subsequent dates, SRCM compared the satellite-derived SC change maps to the SPHY SC change maps. Cells that were of equal value in both change maps indicated that the satellite-observed SC change was also simulated by SPHY. Hence, in cells where SC had appeared on the satellite imagery and snowfall was simulated by SPHY, the snow deposition mechanism in that cell was classified as snowfall. Conversely, in cells where SC had disappeared from the satellite imagery and snowmelt was simulated by SPHY, the snow removal mechanism in that cell was classified as snowmelt. This way, SRCM used the SPHY results as reference data to classify areas of snowfall and snowmelt on the satellite-observed SC changes.

3.5.3 Classification of avalanching

The ASI threshold between the moderate and high susceptibility classes was used as the input parameter (Section 3.4). For each pair of subsequent dates, SRCM evaluated the criteria for gravitational snow removal and deposition separately for each cell.

In cells where SC had disappeared from the satellite imagery and the ASI value was above the threshold, the snow removal mechanism was classified as avalanching. The classification of snow deposition by avalanching requires consideration of multiple factors. Ideally, these factors include flow directions, flow accumulations and snow depths to accurately represent avalanche flow paths, much like the existing SnowSlide model (Bernhardt & Schulz, 2010b). However, this is computationally intensive as each factor must be evaluated per cell and date. For computational efficiency, SRCM approximated potential avalanche deposits based on the watershed, elevation and travel distance.

Four criteria were evaluated to classify whether the snow deposition mechanism was avalanching. If, (1) in a single time step, SC had appeared on the satellite imagery in a cell that is (2) within the same watershed, (3) at a lower elevation and (4) within a maximum travel distance of 1500 m of an avalanche source area, the snow deposition mechanism in that cell was classified as avalanching. The avalanche source area is the lowest cell where avalanche removal has been classified in the same watershed as the

evaluated cell. The travel distance was calculated by subtracting the distance to the watershed outlet of the evaluated cell from that of the avalanche source area.

3.5.4 Classification of eolian snow redistribution

Entrainment of snow particles by wind occurs above a threshold wind speed, which depends on the age and wetness of the snowpack (He & Ohara, 2017; Li & Pomeroy, 1997). A threshold of 4 m/s was used as the minimum wind speed for snow entrainment, based on the lower limit of 95% confidence found by Li and Pomeroy (1997). To identify locations of wind-driven snow deposition and removal, SRCM evaluated each cell against three criteria based on the wind fields and the topographic exposure maps.

In cells where (1) SC had disappeared from the satellite imagery, (2) the wind speed was above the threshold and (3) the topographic exposure in the corresponding wind direction was above average (i.e. exposed), the snow removal mechanism was classified as wind-driven snow removal. Conversely, in cells where (1) SC had appeared on the satellite imagery, (2) the wind speed was below the threshold and (3) the topographic exposure in the corresponding wind direction was below average (i.e. sheltered), the snow deposition mechanism was classified as wind-driven snow deposition.

As only 647 images were available for the 1461 days of interest, subsequent images were often separated by more than one day. In these cases, SRCM not only considered the wind speeds and directions of the subsequent dates but also of the intermediate dates. The maximum wind speed of these dates and the corresponding wind direction were then used to evaluate criteria 2 and 3. This is because eolian snow removal often occurs in relatively short-lived, local gusts (Ágústsson & Ólafsson, 2004). Thus, the maximum wind speed is a better predictor of eolian snow removal than, for example, the mean wind speed.

3.5.5 Classification of multiple or unexplained snow redistribution mechanisms

SRCM's classification scheme included the possibility that a single cell satisfied the criteria of multiple redistribution mechanisms. In this case, SRCM could not determine which mechanism had actually taken place and assumed that the probability of each of the mechanisms having occurred was equal. This assumption is related to the binary nature of SRCM's classifications: each mechanism is assigned a probability of either 1 (possible) or 0 (not possible), based on the criteria described above. Determining fractional probabilities for individual or multiple mechanisms would require more advanced classification criteria. The simplicity of a binary probability was preferred for this study due to time constraints.

In cells where SC had appeared on the satellite imagery, but the criteria for snow deposition were not satisfied, the snow deposition mechanism was classified as unknown. Contrarily, in cells where SC had disappeared from the satellite imagery, but the criteria for snow removal were not satisfied, the snow removal mechanism was classified as unknown.

3.5.6 SRCM output

By iterating over all 646 pairs of subsequent images and evaluating each cell against the criteria for the snow redistribution mechanisms, SRCM generated 646 8-band rasters of the study domain. The bands contained the binary classification maps for each snow redistribution mechanism: (1) snowmelt, (2) removal by avalanching, (3) removal by wind, (4) unexplained removal, (5) snowfall, (6) deposition by avalanching, (7) deposition by wind and (8) unexplained deposition. These results were exported as multiband georeferenced raster files.

The 646 snow redistribution maps were aggregated per month and for the entire study period (2017-2020). This was done by counting the number of occurrences of eolian snow redistribution per cell. Aggregation of band 3 resulted in 13 frequency maps of eolian snow removal: one for each month and one for the 2017-2020 period. Likewise, aggregation of band 7 resulted in 13 frequency maps of eolian snow deposition.

4 Results

4.1 Wind fields and topographic exposure

The daily domain-averaged maximum wind speed and corresponding wind direction, as derived from ERA5-Land for 2017-2020 and used as input for WindNinja, are shown in Figure 4. From January until April, northwesterly winds are dominant and relatively strong. In May and June, the wind speeds decrease and the wind direction becomes more variable, turning towards the southeast and the southwest. During the monsoon season (July until September), southwesterly winds prevail and the wind speeds are lowest. The transition to winter is characterized by increasing wind speeds and a variable wind direction, with winds coming from all intercardinal directions, but mainly southwest and northeast. From November to December, northeasterly winds dominate and wind speeds reach their annual maxima.

The downscaled wind fields from WindNinja show considerably higher local wind speeds than the domain-averaged input values, indicating topographical flow acceleration (Figure 5). Wind speeds are high (12-20 m/s) on ridges and exposed locations and low (0-4 m/s) in valleys and sheltered locations (Figure 5; Figure 6). Also, the extreme relief of the study area causes flow reversal effects on the leeward sides of mountains. Overall, the downscaled wind fields resemble the domain-averaged input data. Across the study domain, the downscaled wind speeds are highest in April-May and November-December and lowest during the monsoon season, much like the domain-averaged input wind speeds.
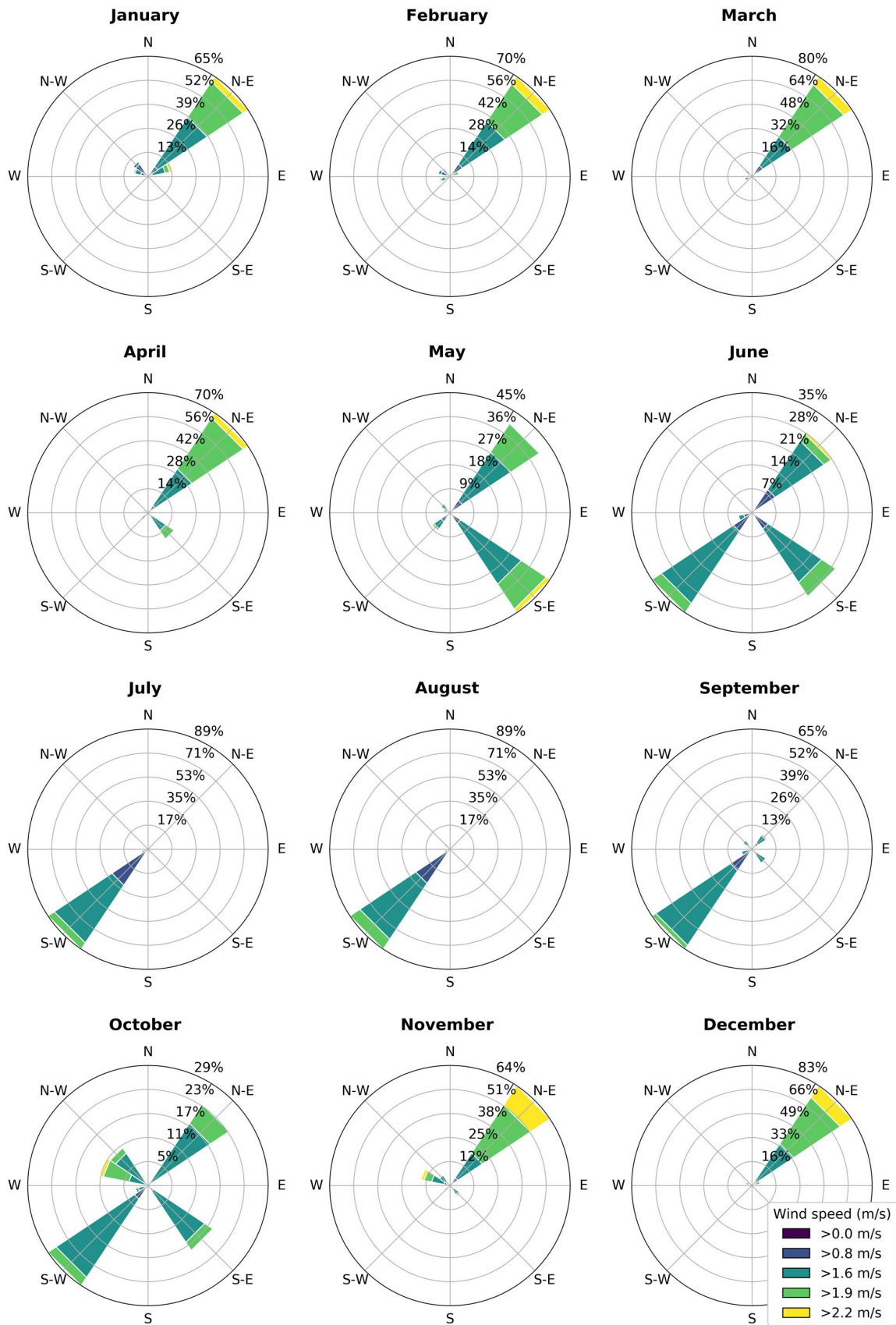
Figure 4: Wind roses of domain-averaged daily maximum wind speeds per month of the year for 2017-2020. Note that the frequency of occurrence, displayed on the concentric circles, is not constant.
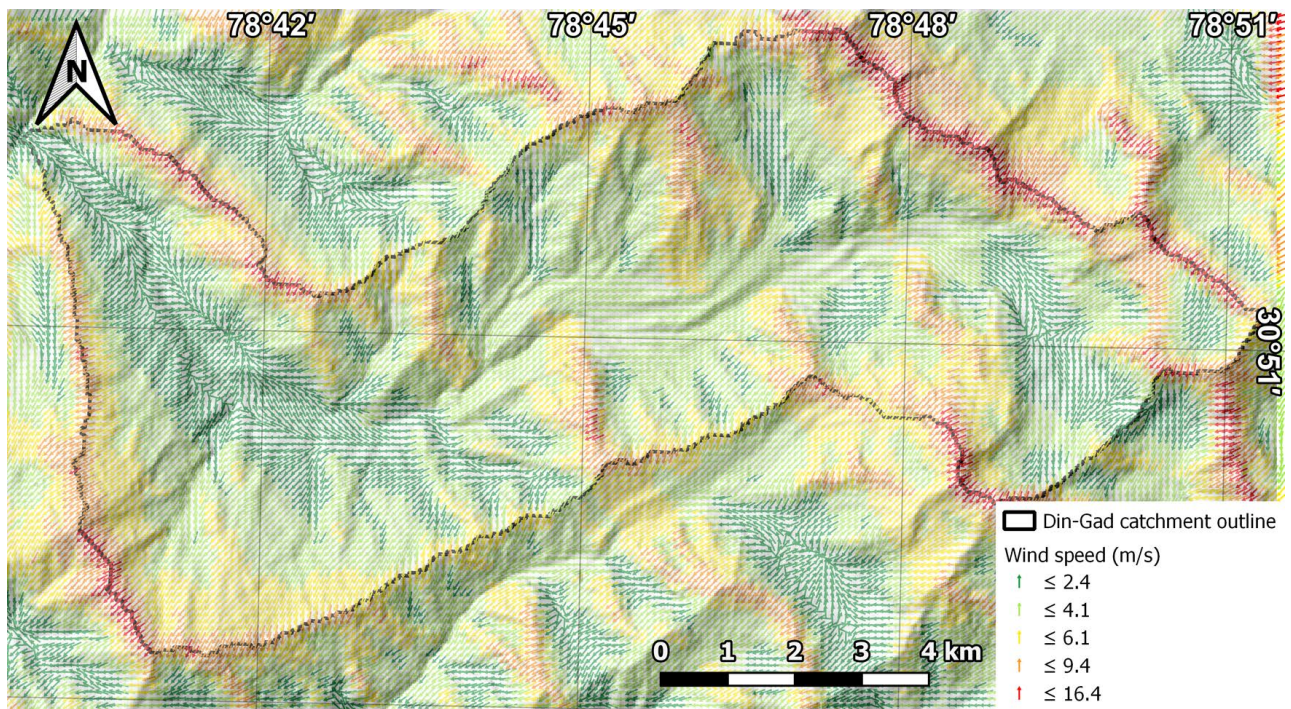
Figure 5: Downscaled wind field for January 9, 2017. Wind vectors are shown as arrows, pointing in the direction the wind is blowing towards. Vector colors indicate wind speed. This wind field was produced by WindNinja using the mass conservation solver and domain-averaged wind speed and direction input values of 1.9 m/s and 47.7 degrees (where $0°$ is north), respectively. These initial conditions represent the year-round dominant wind conditions.
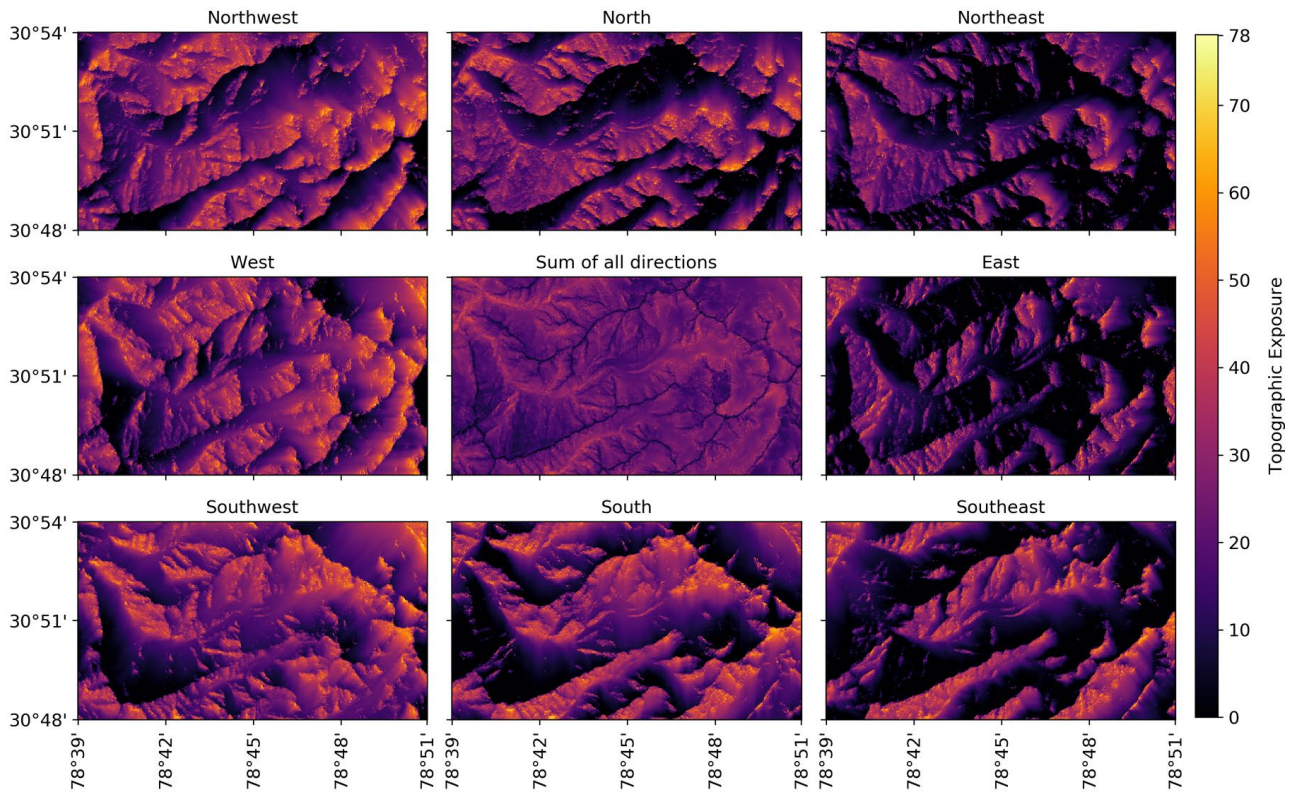
Figure 6: Topographic exposure for each (inter)cardinal wind direction and as the sum of all directions. High values indicate exposed locations, low values indicate sheltered locations.

4.2 Avalanche susceptibility maps

Over the 2017-2020 period, almost all cells in Din-Gad Catchment have encountered snow cover at least once. The per-cell mean ASI of all dates thus covers the entire study domain, representing the ASI map of the study area if all cells were snow-covered (Figure 7). The positive relation between ASI and elevation is apparent, with the majority of the high-susceptibility class occurring in the higher-altitude eastern part of the catchment. The hillshade overlay and contour lines in Figure 7 illustrate the texture of the terrain and the positive relation between slope and ASI. The steep slopes in the high-relief eastern areas are most susceptible to avalanching, whereas the valley bottoms show minimal susceptibility. The ASI threshold between moderate and high susceptibility was found to be 6.69.
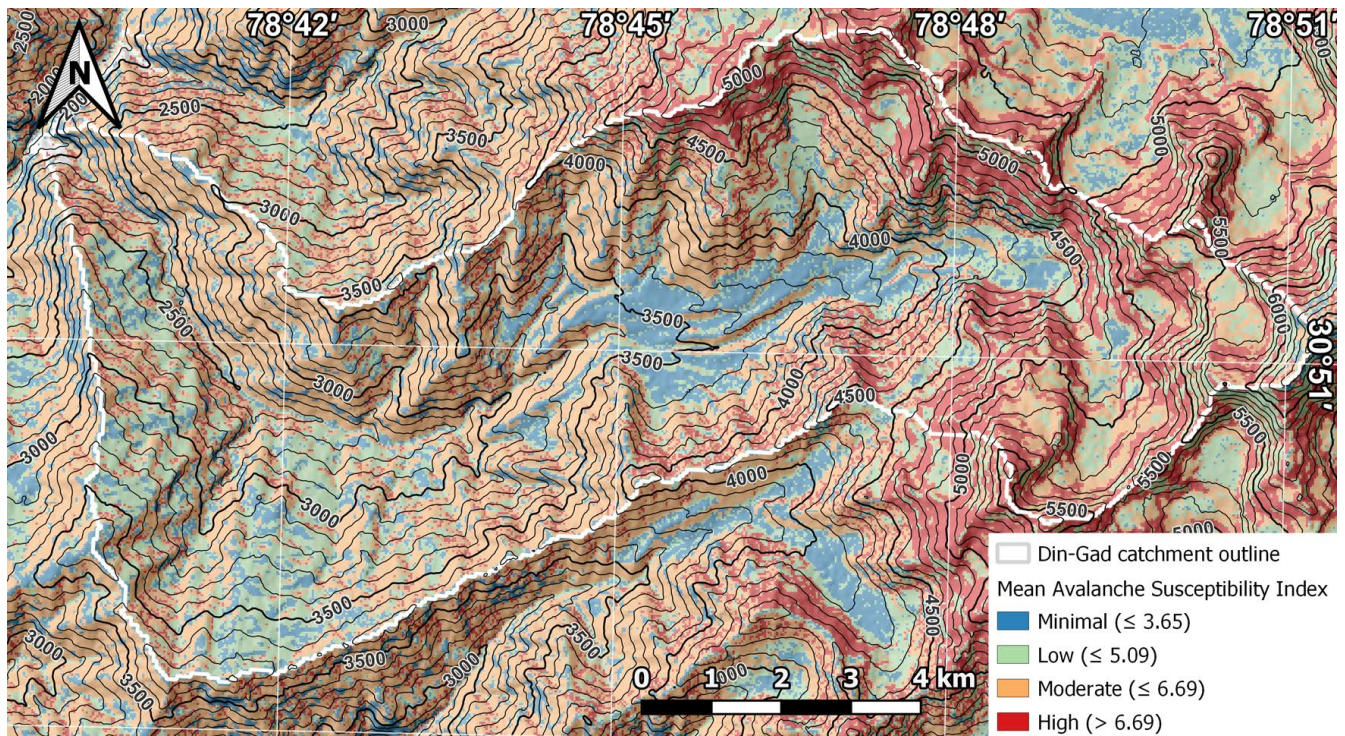

Figure 7: Map of mean Avalanche Susceptibility Index in Din-Gad Catchment.

4.3 SRCM results

In the study period, 4,541,962 cells with SC change were identified from the satellite imagery. Of these cells, 2.6% were classified by SPHY using the model parameters described in Section 3.3. 35.8% of SC changes were classified by SRCM and 61.6% were not classified at all (Figure 8). This means that in 61.6% of the cells, the snow cover, wind conditions and topographical parameters did not satisfy SRCM's criteria for any of the redistribution mechanisms. Of all SC changes, 2,212,793 cases were classified as snow removal and 2,329,169 as snow deposition. A simple two-tailed test with a significance level of 0.05 shows that this difference is significant.

In terms of snow removal, 14.4% of SC changes were attributed to wind-induced removal, 22.7% to avalanching, 2.5% to melting and 60.4% were unexplained by SRCM. Regarding snow deposition,

28.5% of changes were attributed to wind-supplied deposition, 6.1% to avalanching, 2.7% to snowfall and 62.7% were unexplained. Notably, almost 1.6 times as much snow removal was attributed to avalanching than to wind-driven removal. In contrast, wind-supplied snow deposition was classified almost 4.7 times as frequently as deposition by avalanching. Trial and error inspection of several satellite images of days where SRCM classified abundant avalanching revealed no evidence of avalanches. Most SC changes generally occurred during October, November and December, except for in 2019, when most changes occurred in January, March and April (Figure 8).
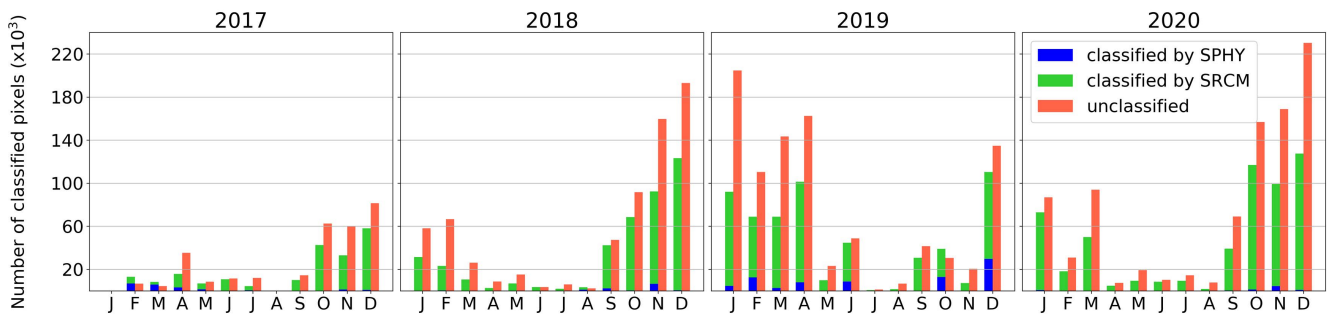

Figure 8: Bar chart displaying the number of cells where SC change took place (both snow removal and deposition), per month for 2017-2020. Each month displays two bars: the left bar denotes the number of cells that were classified by a model (the cell count for SRCM is stacked upon the SPHY cell count); and the right bar denotes the number of cells that were not classified by any model.

On average, the SRCM classification maps depict the SC changes that occurred during roughly two days. The maps show distinguished patterns between the snow redistribution mechanisms. Time steps where either snow removal or deposition persists are abundant and cases where both occur on the same day are rare. Locations where SRCM identified multiple possible mechanisms in the same cells are also rare. These cases mostly represent a shared probability between snowfall and wind-supplied snow deposition or between snowmelt and wind-driven snow removal.

4.3.1 Examples of SRCM output maps

Evaluation of the SRCM results using PlanetScope imagery reveals that SRCM can classify larger areas of SC change than SPHY, although the redistribution mechanisms are often incorrectly classified. For example, a considerable portion of the study domain received snow on April 15, 2019, of which 29.4% were classified by SRCM, whereas only 11.6% were classified by SPHY using the chosen model parameters. 59.0% of the observed SC change was not classified by SRCM on this date (Figure 9). Examination of the southwestern ridge reveals that the cells where snow deposition by avalanching is classified, are likely incorrect due to the absence of lobes or recognisable avalanche deposits (Figure 9). Furthermore, there are no cells on the upper part of the ridge that were classified as possible avalanching sites on April 15, 2019.
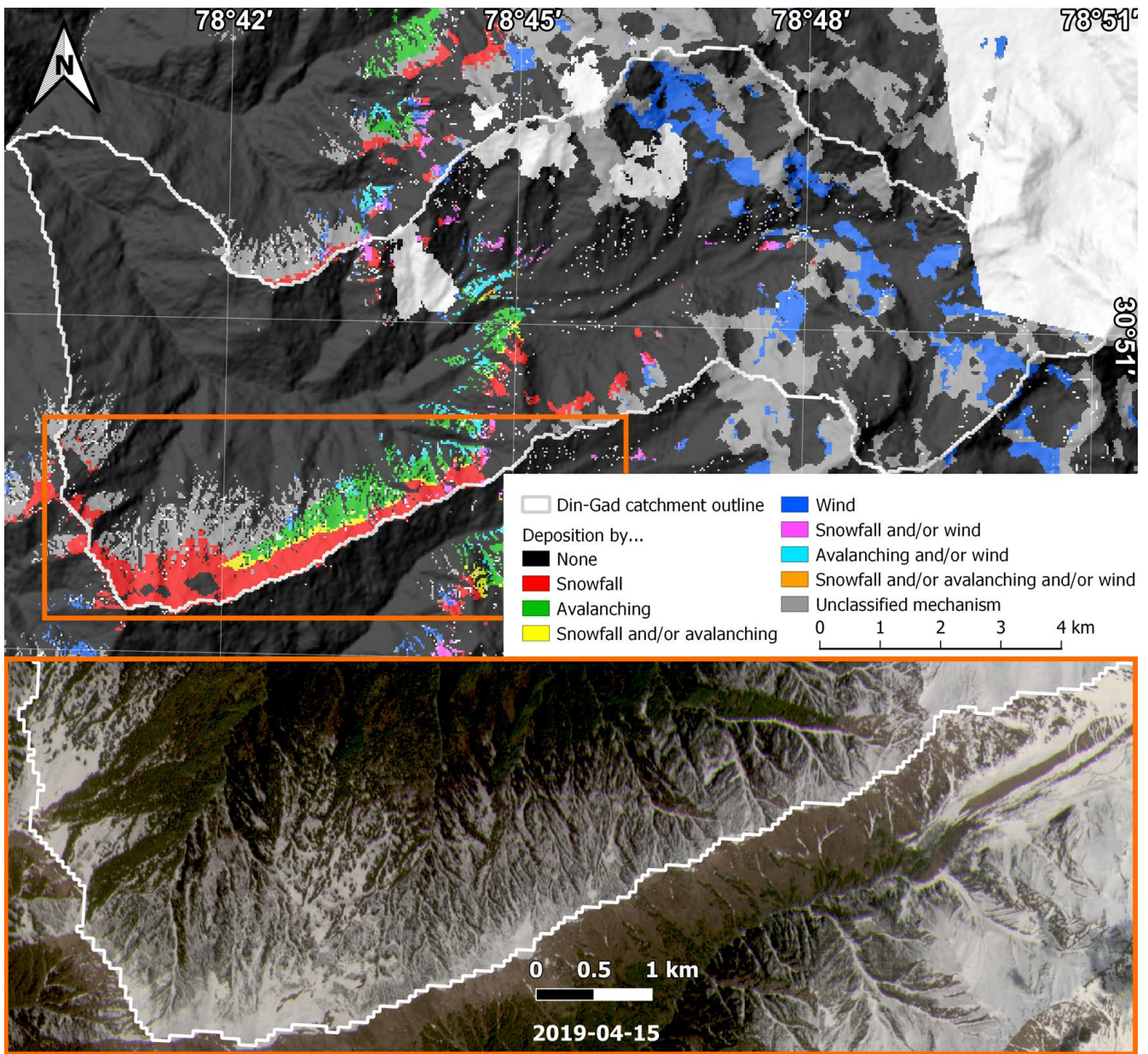
Figure 9: SRCM results for April 15, 2019. Cells are colored according to the snow deposition mechanism. Snow removal is not shown, as it was negligible on this date. The lower part of the figure shows a PlanetScope image (3 m resolution) covering the extent of the orange rectangle.

Between October 27 and 28, 2020, large areas of snow cover disappeared from the high, eastern part of Din-Gad Catchment (Figure 10). SRCM classified 53.9% of this SC change, whereas the other 46.1% remained unclassified. Notably, SPHY did not simulate any SC removal during this day. It is important to note that SPHY may have simulated snowmelt of less than 5.0 mm but this is not considered as SC removal using the chosen model parameters. Whereas SRCM attributed most snow removal to avalanching, the satellite images do not display any evident scarps, break lines or other avalanche-related features.
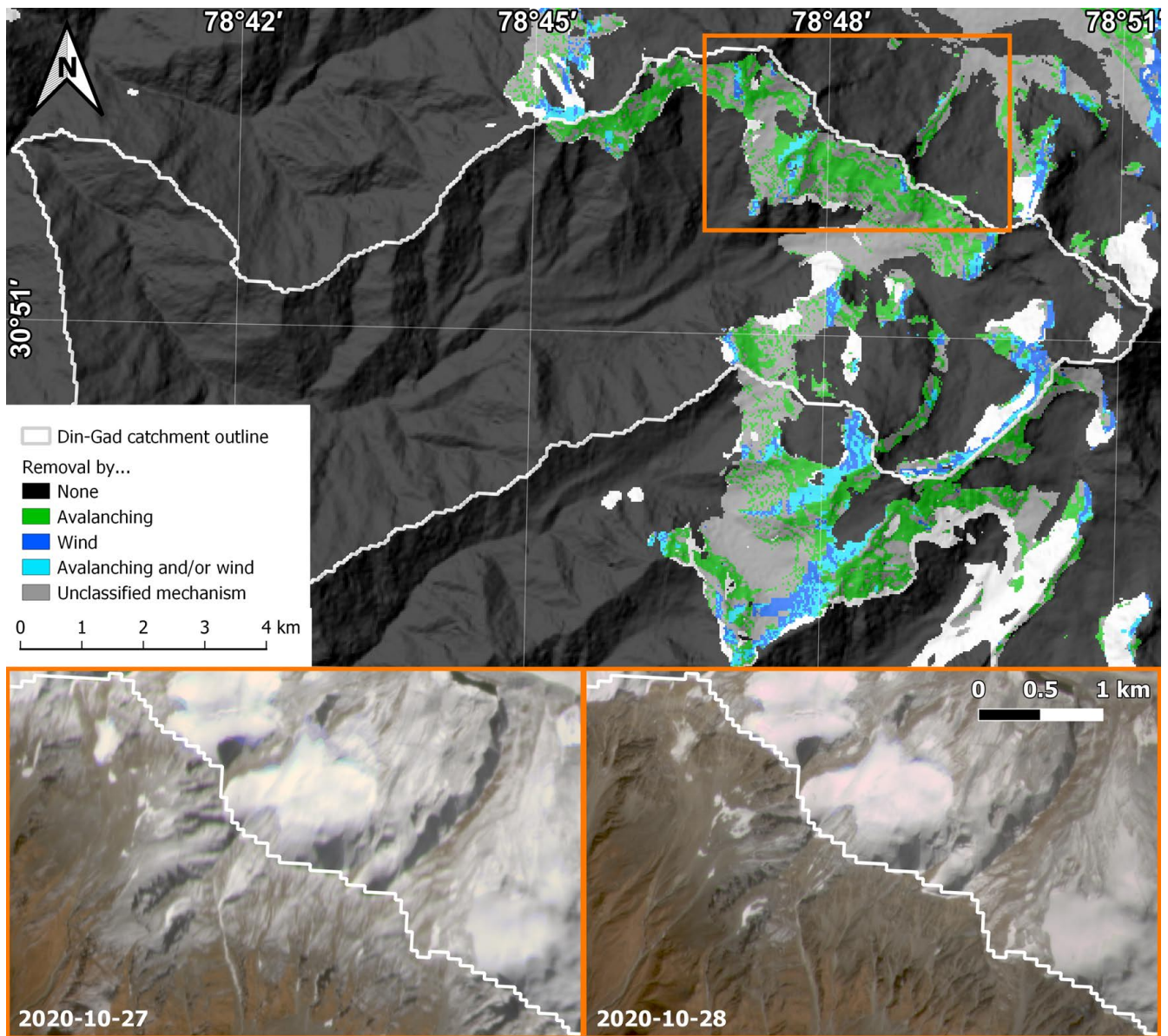
Figure 10: SRCM results for October 28, 2020. Cells are colored according to the snow removal mechanism. Snow deposition did not occur on this date and the mechanisms shown in the legend are the only ones that were classified on this date. The lower part of the figure shows PlanetScope images of the before and after situation in the left and right panel, respectively. These images cover the extent of the orange rectangle.

4.3.2 Relation between wind speed and frequency of eolian snow redistribution

Figure 11 illustrates the relation between wind speed and the frequency of wind-induced snow removal. From January until April and in June, the correlation is generally negative and significant, meaning that the frequency of occurrence decreases with increasing wind speed. In May, the negative correlation is only significant for 2020. July, August and September generally show insignificant or variable correlations and in October, a significant positive correlation appears. Thus, in October, the frequency of occurrence increases with increasing wind speed. In November, the correlation is significant but variable over the years. In December, the significant negative correlation returns.

2020 is the year where most months show a significant correlation, resulting in a pronounced pattern (Figure 11). From December until May, the correlation is negative and significant. A subtle trend is visible during the first five months of 2020. From December until March, wind speeds of 5-7 m/s show snow removal frequencies of at least 0.9. In April and May, these frequencies are found at slightly higher wind speeds (6-8 m/s). This trend continues in June and July, although the correlation in these months is insignificant. During the late monsoon season and fall (September until November), frequency of eolian snow removal increases with increasing wind speed. Also, the highest frequencies (>0.9) in these months are found at wind speeds above 12 m/s. This indicates that the threshold wind speed for blowing snow is seasonally variable.
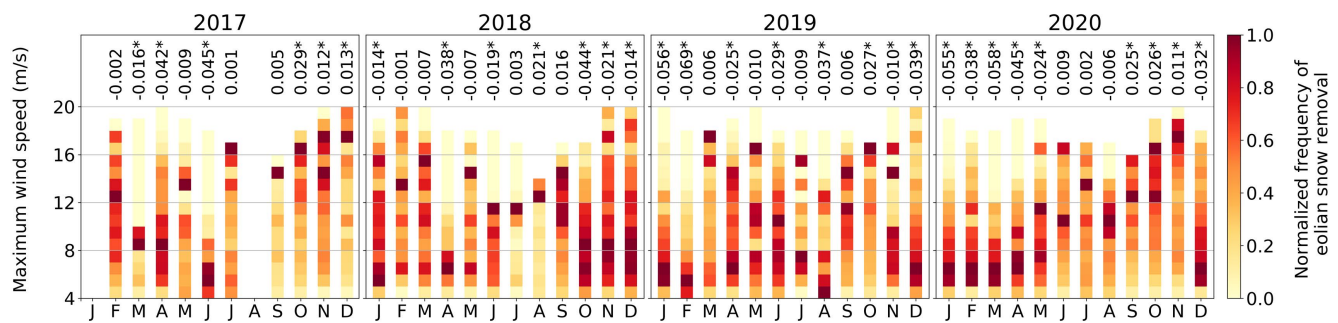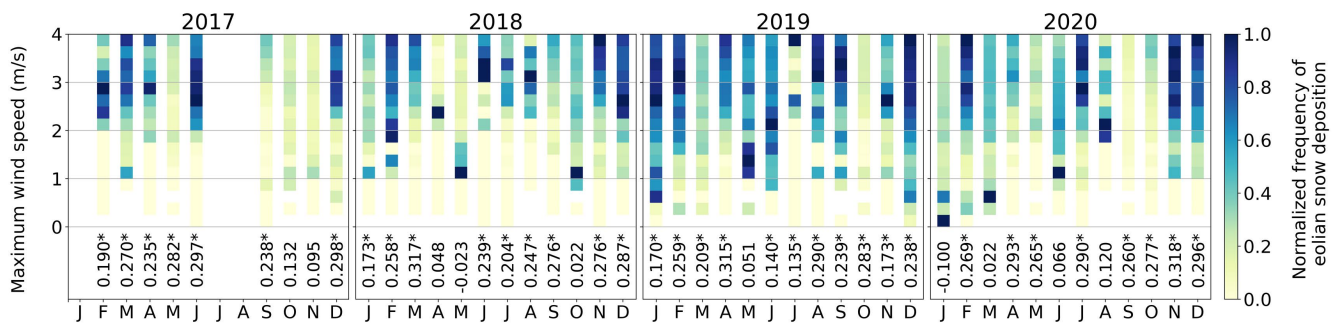

Figure 11: Binned scatterplot of maximum wind speeds and frequency of eolian snow removal per month for 2017-2020. Each column represents 230,318 maximum wind speed values: one per cell in the study domain of 638x361 cells. The wind speeds are grouped into bins of 1 m/s and the color represents the mean normalized frequency of eolian snow removal per bin. Above each column, the regression coefficient of a linear regression of frequency on wind speed is displayed. Asterisks indicate a significant correlation, assuming a significance level of 0.05. Note that January and August of 2017 show no values due to the absence of suitable images for these months.

Figure 12 shows that the frequency of eolian snow deposition generally decreases with decreasing wind speed, as 35 of the 48 months show a significant positive correlation. Of the 28 months that show deposition frequencies of at least 0.9 at any wind speed, 18 months show these frequencies at wind speeds above 2.5 m/s, of which 11 months show these frequencies at speeds over 3.0 m/s. In other words, high frequencies of deposition (>0.9) occurs over 1.5 times as often at wind speeds of 2.5-4.0 m/s than at speeds of 0.0-2.5 m/s. Notably, there are no months that show a significant negative correlation.

4.3.3 Patterns of eolian snow redistribution

The general patterns of eolian snow redistribution (Figure 13) reflect the northeast topographic exposure (Figure 6), which corresponds to the year-round prevailing wind direction (Figure 4). The highest snow removal frequencies are concentrated on exposed, northeast-facing ridges (Figure 13). The highest snow deposition frequencies occur in sheltered areas downwind of these ridges. The frequency of wind-supplied snow deposition generally decreases from east to west, with decreasing elevation.

Figure 12: Binned scatterplot of maximum wind speeds and frequency of eolian snow deposition per month for 2017-2020. Each column represents 230,318 maximum wind speed values: one per cell in the study domain of 638x361 cells. The wind speeds are grouped into bins of 0.25 m/s and the color represents the mean normalized frequency of eolian snow deposition per bin. Below each column, the regression coefficient of a linear regression of frequency on wind speed is displayed. Asterisks indicate a significant correlation, assuming a significance level of 0.05. In July, 2017, no eolian snow deposition was classified. January and August of 2017 show no values due to the absence of suitable images for in these months.
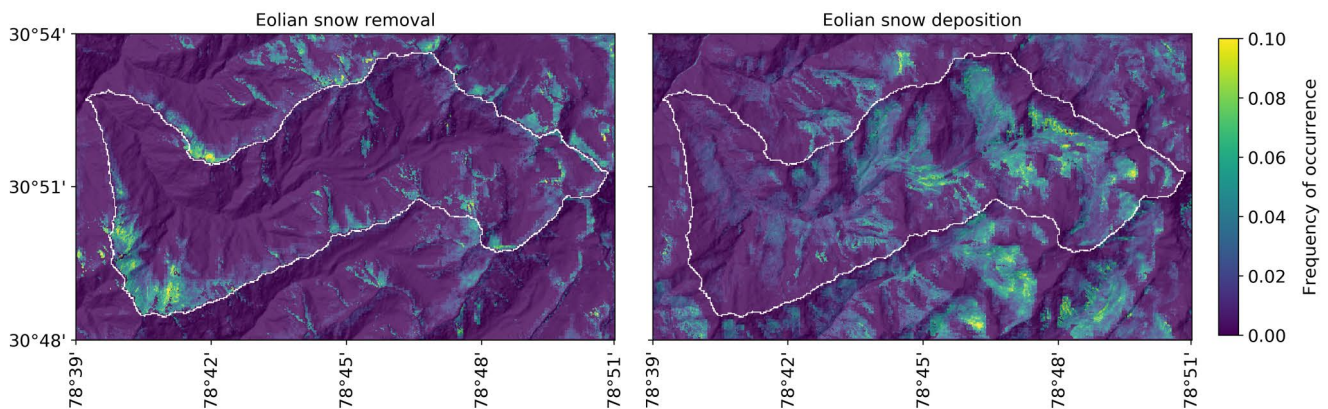
Figure 13: Maps showing the year-round frequency of occurrence of eolian snow removal (left) and deposition (right) in the study domain. Din-Gad Catchment is outlined in white.

The monthly maps of wind-driven snow removal (Figure 14) and snow deposition (Figure 15) also show a clear relation with topographic exposure (Figure 6). Exposed areas experience more frequent wind-induced snow removal, whereas sheltered areas experience more snow deposition. These patterns are consistent with the dominant wind directions per month (Figure 4).

Wind-induced snow removal patterns

From January until April, wind-driven snow removal is concentrated in mostly the same locations in the study domain (Figure 14). These are northeast-facing slopes close to the ridges that demarcate the catchment boundary in the southwest and northwest of the study area. These faces are exposed in the prevailing wind direction during these months (Figure 4; Figure 6). Along the more elevated northeastern boundary of Din-Gad Catchment, patches of frequent eolian snow removal can also be identified.

May and June show relatively little wind-blown snow removal due to decreased wind speeds (Figure 14, supported by Figure 4). Also, areas of activity are less distinguished due to the more variable wind direction. July and August display large areas of NoData values (Figure 14; Figure 15). This is related to the extensive cloud cover during the monsoon season, resulting in limited availability and coverage of satellite images for these months (Figure 2). Therefore, the highest frequencies for July and August are less reliable than for the other months.

During the end of the monsoon season in September, the gentle southwesterly winds limit the eolian removal of snow to the most exposed southwest-facing slopes (Figure 14, supported by Figure 4; Figure 6). The variable wind direction in October results in a more erratic pattern of wind-induced snow removal activity. From November to December, the strong northeasterly winds result in areas of frequent wind-driven snow removal that are concentrated on exposed, northeast-facing slopes.

Figure 14: Maps showing the frequency of occurrence of eolian snow removal per month in the study domain. Din-Gad Catchment is outlined in white. Black pixels indicate NoData.

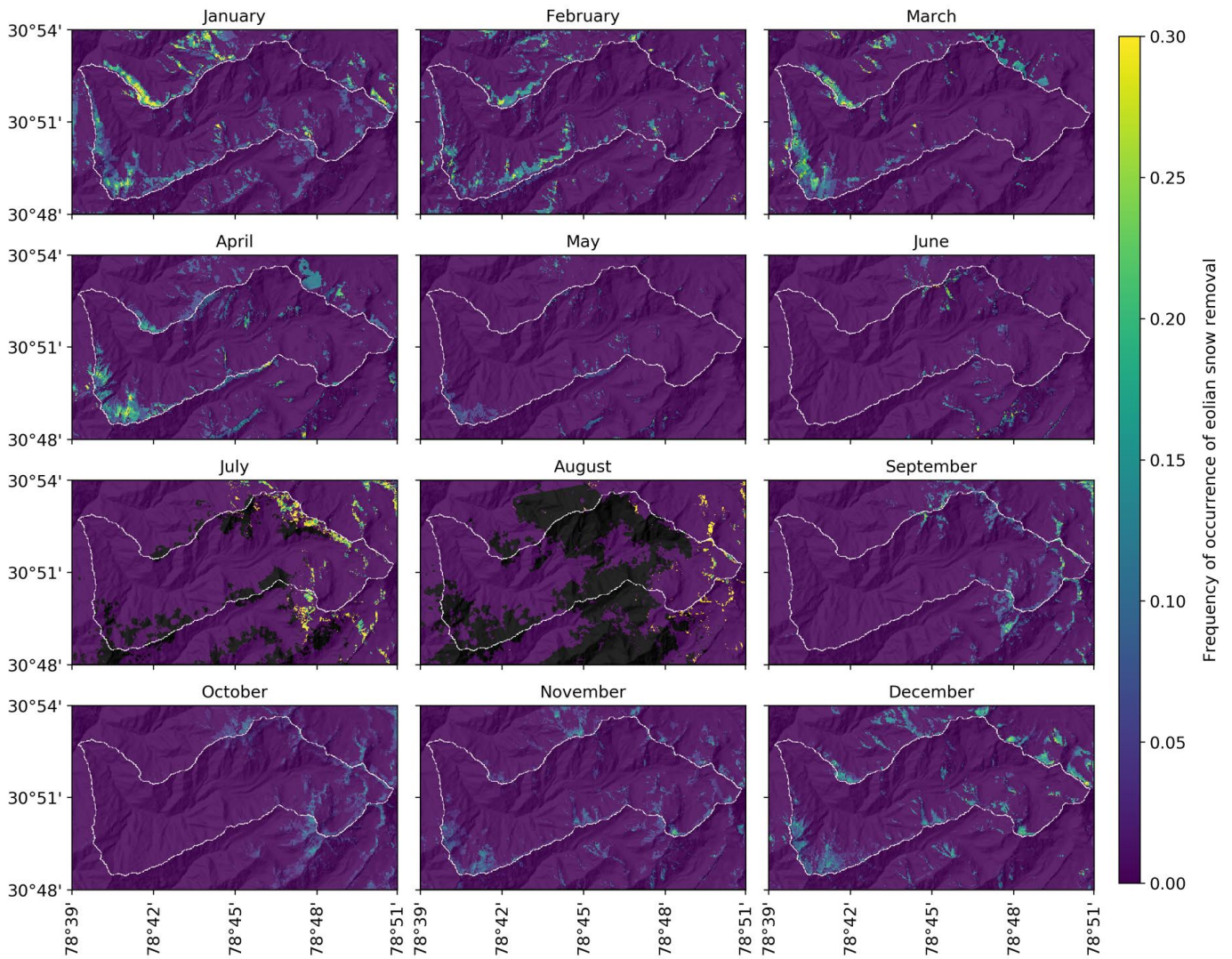**Wind-supplied snow deposition patterns**

In general, the eolian deposition of snow occurs over more widespread areas than removal does (Figure 15). When supported by Figure 4 and Figure 14, Figure 15 shows another pattern. In the western half of the catchment, eolian snow deposition occurs in the valleys and on the lee sides of the mountains, downwind of areas of frequent snow removal. This pattern is most pronounced in January and March and to a lesser extent in February. In the eastern half of the catchment, the frequency of deposition decreases from January to March (Figure 15). In January, local concentrations of frequent deposition are observed on the exposed, northeast-facing slopes just southwest of the Dokriani glacier (Figure 15, supported by Figure 6). In February, deposition is concentrated towards the valley center.

Despite the similarity of wind conditions between March and April (Figure 4), the deposition of snow is more erratic and towards the higher elevations in the east during April (Figure 15). In May and June, limited snow is available for deposition, resulting in relatively low frequencies of eolian snow deposition.
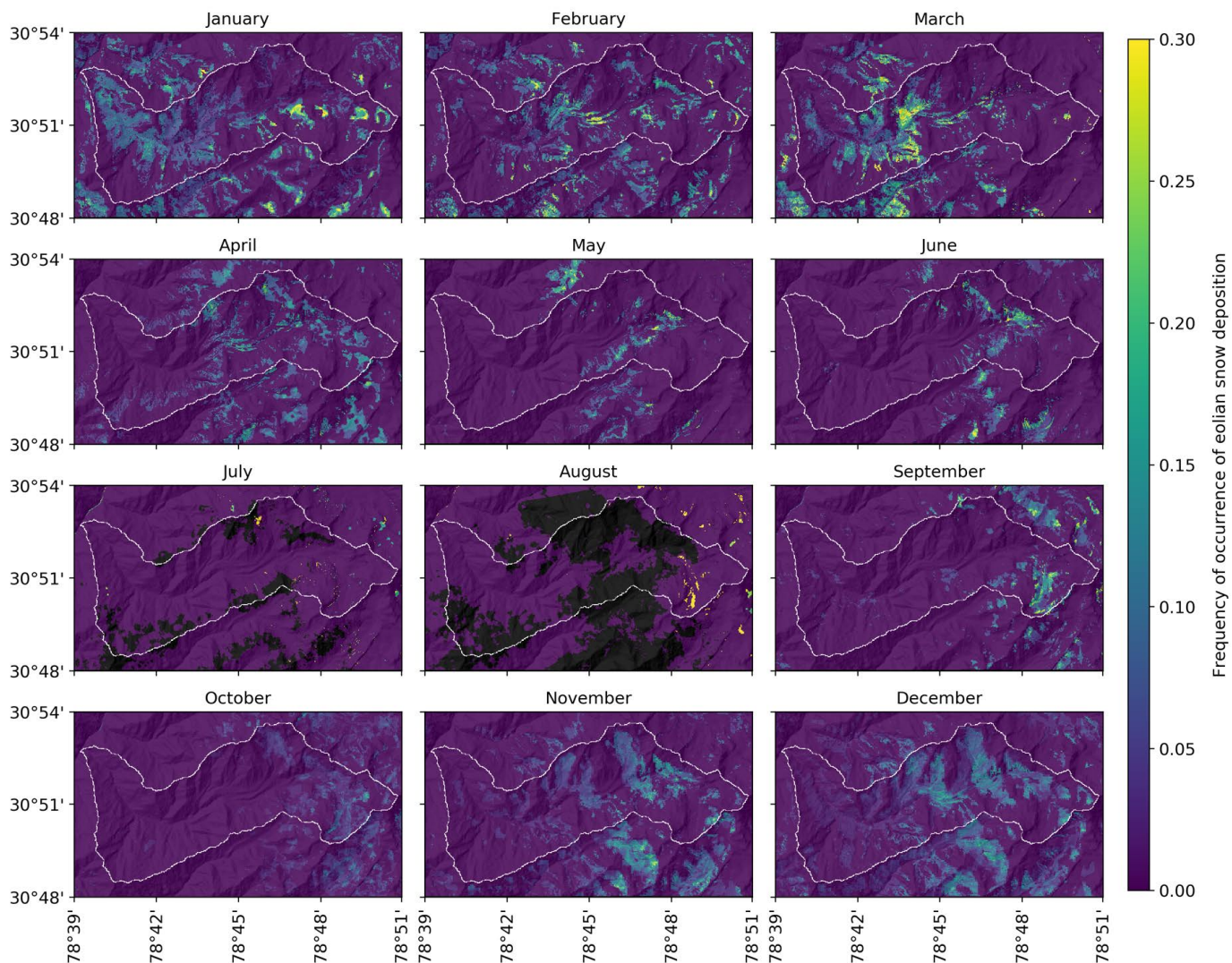
Figure 15: Maps showing the frequency of occurrence of eolian snow deposition per month in the study domain. Din-Gad Catchment is outlined in white. Black pixels indicate NoData.

During the late monsoon season, deposition is concentrated in topographically sheltered areas that face away from the prevailing wind direction (Figure 15, supported by Figure 4; Figure 6). Snow that is eroded from southwest-facing slopes is deposited on opposite-facing slopes, just southwest of the Dokriani glacier and just outside of Din-Gad Catchment, in the northeastern corner of the study area (Figure 15). In October, the variable wind conditions again result in an erratic pattern of deposition. As is the case for the snow removal patterns, the deposition patterns in October are restricted to the more topographically extreme parts of the catchment, where topographic exposure gradients and wind speed gradients are the greatest.

November and December experience the highest frequencies of wind-supplied snow deposition of the year (Figure 15). Contrary to the patterns of wind-induced snow removal in these months, the deposition patterns are widespread and located in the valleys and sheltered areas downwind of the snow removal areas (Figure 15, supported by Figure 4; Figure 6; Figure 14). Remarkably, the most concentrated areas of high wind-driven snow removal frequency in December are contrasted by the diffuse patterns of high wind-supplied snow deposition frequency. Also, the frequency of deposition in December decreases downwind (towards the southwest), with increasing distance from the potential source areas.

5 Discussion

5.1 Accomplishments of this study

This study has demonstrated a novel method of mapping eolian snow redistribution patterns in complex topography. An unprecedented combination of optical satellite imagery, downscaled wind fields and an empirical classification model was used. The processing of Sentinel-2, Landsat 8 and PlanetScope images on the flexible and scalable Earth Engine platform provided a solid base for mapping near-daily SC change at 30 m resolution. Although the spatial coverage was inherently limited by cloud cover, the studied period (2017-2020) was long enough to provide almost full coverage of the study area by monthly averaging the data.

This is the first time that WindNinja, an application originally developed for wildland fire modelling, was used for modelling snow redistribution. With the ERA5-Land input data, it provided precise downscaled wind fields, even for the extreme Himalayan topography. Few researchers outside of the WindNinja development team have used the application for scientific purposes (Keenan et al., 2022; Mallare et al., 2022; Reynolds & Lundquist, 2019). The application was an essential component of this study that provided valuable information on the dynamics of wind and wind-blown snow over complex terrain.

The newly developed Snow Redistribution Classification Model (SRCM) demonstrated the ability to identify SC changes from satellite imagery and classify three possible snow removal or deposition mechanisms responsible for these changes. The model explored the feasibility of empirical snow redistribution modelling with a modest to low computational demand. Given sufficient data availability and compu-

tational resources, SRCM itself is scalable to study domains and time steps of any size. The scalability limits of this study are not determined by SRCM, but rather by the satellite image availability and WindNinja. Although SRCM has its limitations, which are discussed in Section 5.5, it provides a new concept for studying eolian snow redistribution over complex topography at high spatiotemporal resolution.

5.2 Comparison of WindNinja algorithms

The ERA5-Land wind data was downscaled using the mass conservation solver in WindNinja, resulting in wind fields that resemble the initial domain-averaged wind field (Section 3.2.1). Nevertheless, the mass-momentum conservation solver is theoretically more suitable for Din-Gad Catchment, because it accounts for incompressible turbulent flow and momentum effects. This is especially important in study areas with extreme topography. However, this study was limited to the mass-momentum solver due to constraints on time and computational resources. Moreover, ERA5-Land climate reanalysis data is designed to provide an accurate approximation at scales much larger than Din-Gad Catchment. For reference, only six cells of the ERA5-Land grid intersect with the study domain. Arguably, more realistic results could be generated by initializing WindNinja using AWS wind measurements, although multiple AWS would be necessary. Despite the presence of an AWS in Din-Gad Catchment, its data was not accessible at the time of this study.

A comparison was made between the mass and mass-momentum conservation solvers. Figure 16 shows the downscaled wind field for January 9, 2017 (as does Figure 5), but generated using the mass-momentum solver. The differences are prominent: the mass-momentum solver (Figure 16) yields less variable wind speeds, but more variable wind directions compared to the mass solver (Figure 5). For example, the maximum factor of topographical flow acceleration (the maximum downscaled wind speed divided by the initial domain-averaged wind speed) is lower for the mass-momentum solver (ca. 4.9) than for the mass solver (ca. 8.6). The domain-averaged downscaled wind speeds are 4.0 m/s for the mass solver and 2.1 m/s for the mass-momentum solver, resulting in mean topographical flow acceleration factors of 2.1 and 1.1, respectively. This is in line with the mean factors of 1.7-2.1 found by other studies, albeit for less extreme topography (Bowen & Lindley, 1974; Ngo & Letchford, 2009).

Differences in downscaled wind direction are also abundant, reaching up to 90° on the northeast-facing slopes in the southwest of the catchment and even up to 180° in the central valley of the catchment (Figure 5; Figure 16). Finally, the downscaled wind field from the mass-momentum solver shows more pronounced turbulent effects on the lee side of topographical obstacles, that often take the shape of eddies, whereas this is generally not the case for the mass conservation solver.

The large differences in downscaled wind speed and direction imply that if the mass-momentum solver was used in this study, the resulting snow redistribution patterns would be quite different. Firstly, the lower topographical flow acceleration factors indicate that the wind speed threshold for snow transport would be exceeded less often. Hence, eolian snow removal would be more restricted to areas with high acceleration factors, such as the steep ridges along the northeastern boundary of Din-Gad Catchment.
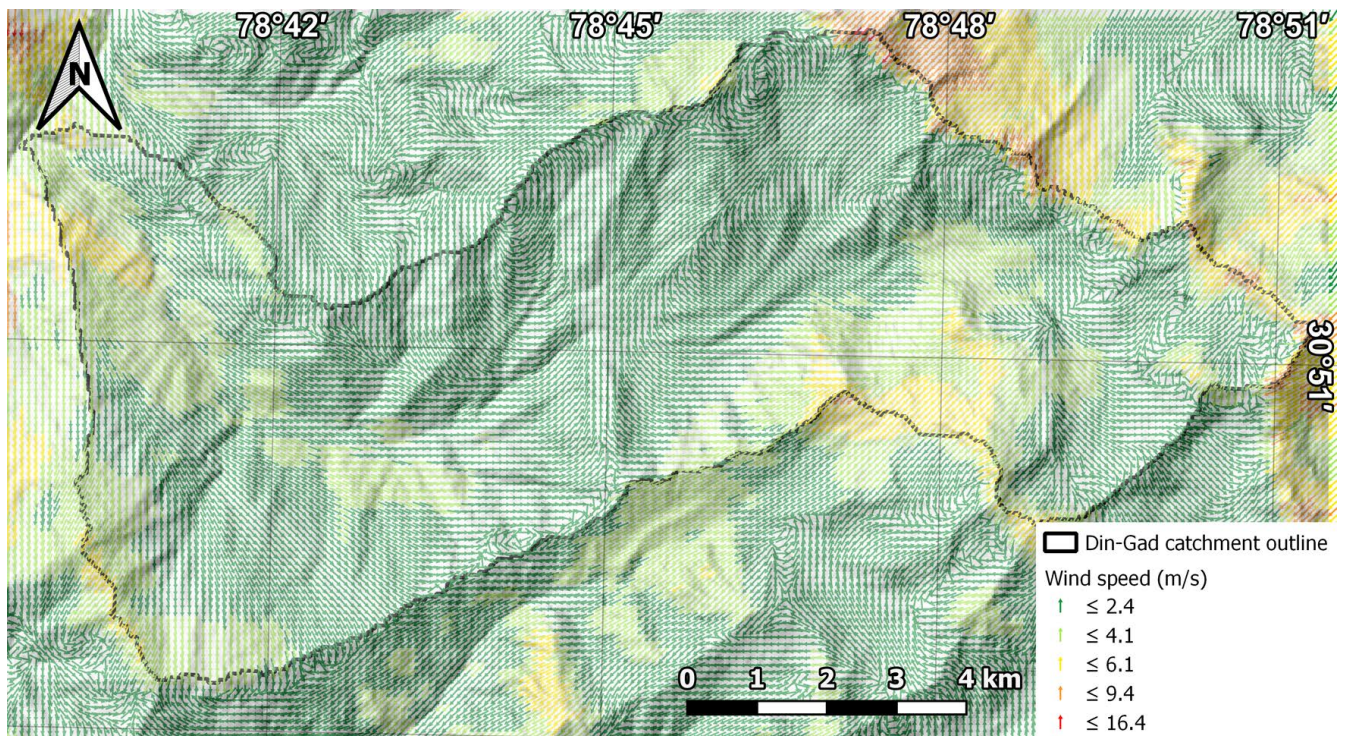
Figure 16: Downscaled wind field for January 9, 2017. Wind vectors are shown as arrows, pointing in the direction the wind is blowing towards. Vector colors indicate wind speed. This wind field was produced by WindNinja using the mass-momentum conservation solver and domain-averaged wind speed and direction input values of 1.9 m/s and 47.7 degrees (where 0° is north), respectively. These initial conditions represent the year-round dominant wind conditions.

Secondly, the more variable downscaled wind directions are more poorly described by the domain-averaged wind direction. As the latter determines the topographic exposure, the relation between the eolian snow redistribution patterns and the topographic exposure in the prevailing wind direction would be weaker. Finally, the more pronounced turbulent effects would lead to stronger wind speed gradients on the lee sides of obstacles, leading to more wind deceleration and faster snow deposition in these areas. This would restrict eolian snow deposition to more sheltered areas and limit the potential travel distance of airborne snow.

These implications emphasize that care should be taken when using downscaled wind fields for modelling snow transport, as snow redistribution models are highly sensitive to wind speed and direction (Bernhardt et al., 2009; Dadic et al., 2010; Eidsvik et al., 2004; Essery, 2001; Liston & Sturm, 1998). However, the uncertainty of the model results can only be quantified with a sensitivity analysis, which is further discussed in Section 5.5.

5.3 Interpretation of snow redistribution mechanisms

5.3.1 Snowfall and snowmelt

The overall SC change classification ratio of 2.6% for SPHY is remarkably low. This is indicative of the limitations of a TI-based snow cover model. Whereas this study only focuses on snow cover, SPHY can

also simulate snow depth. SPHY may perform adequately for large snow depths, but its performance is inadequate for thin snowpacks, as SC change occurs at modest snow depths. In regions where SPHY had difficulty classifying SC change, such as the lower ridge area in the southwest corner of Din-Gad Catchment (Figure 9), SPHY possibly simulated snow deposition up to a depth of 5.0 mm. Below this threshold, cells are modelled as snow-free. Lowering this threshold could increase SPHY's SC change classification ratio, as snowfall and snowmelt of snowpacks less than 5.0 mm would also be classified. However, more extensive research is necessary to quantify exactly how much snow cover change is overlooked by SPHY. This could be done by running the model with different parameter settings and performing sensitivity analyses.

Regarding the low classification ratio, another explanation involves SPHY's temperature input data, which is downscaled from ERA5 data using TopoSCALE (Fiddes & Gruber, 2014). TopoSCALE's simple parameterization of temperature lapse rate is likely too general for the actual temperatures in the study area. This parameterization is especially sensitive to errors around freezing temperature. If the simulated temperature deviates only $1°C$ from the actual temperature, the simulated snow line will deviate 192 m in elevation from the actual snow line. This is assuming a temperature lapse rate of -5.2$°C$/km, which represents annual mean conditions in the Central Himalaya (Kattel et al., 2013). If a $1°C$ error makes the difference between above or below-zero temperatures, areas just below or above the snow line, within a distance proportional to the lapse rate, will be erroneously simulated as snowmelt or snowfall areas. In short, a simple parameterization of temperature lapse rate is insufficient for modelling the full extent of snowfall and snowmelt in complex topography.

Yet another potential cause of SPHY's low classification ratio is the propagation of errors from the downscaled ERA5 input data. ERA5 is designed to provide large-scale (30 km) estimates of climatic variables at an hourly interval. Although vast amounts of historical observations have been assimilated into ERA5's climatic models, the reanalysis data contains uncertainties regarding the magnitude and timing of precipitation events (Hersbach et al., 2020). This is especially relevant for study areas at subgrid scales (i.e. scales smaller than the native 30 km resolution), like Din-Gad Catchment. After downscaling the ERA5 data with TopoSCALE and using it to run SPHY, an uncertainty of a few hours in the timing of a precipitation event (in ERA5) may result in a one-day delay of a snowfall event (in SPHY). Comparison of the SPHY-simulated SC change and the satellite-observed SC change (by SRCM) would then result in an overlooked (non-simulated) SC change on one day (type II error) and a falsely simulated SC change on the next day (type I error).

5.3.2   Avalanching

Figure 9 shows that on April 15, 2019, large areas of snow cover appeared on the southwestern flanks of Din-Gad Catchment. Of the observed SC change, only the upper part of the ridge was identified by SPHY. This demonstrates the shortcomings of the TI-based approach. SRCM neither successfully classified the snow deposition mechanism on the slopes below the ridge. Figure 9 demonstrates that

SRCM can classify unnaturally large areas as potential avalanche deposits without considering the number or size of avalanche source areas on the same day. SRCM's criteria are a crude approximation of potential avalanche deposit areas based on the watershed, elevation and travel distance. These oversimplifications hypothetically allow modelled avalanches to travel obliquely down a uniform slope or grow into disproportional sizes, which is both untrue to reality.

A possible solution would be to limit the number of potential avalanche deposit cells to the number of classified avalanche source cells. However, this would not account for differences in snow depth. In reality, avalanching is highly unlikely to completely remove the snow cover, as the snow slides across a smooth fault surface, which is usually the underlying snow that smoothes out most terrain roughness (Schweizer et al., 2003). Ideally, SRCM's criteria should include flow paths, flow accumulations and snow depths, much like the SnowSlide model of Bernhardt and Schulz (2010b). This would drastically improve the accuracy of the avalanche deposit classifications, although the high computational demand would be disadvantageous for studies over large areas and long periods. The SnowSlide model was not used in this study due to computational limitations. Additionally, the maximum travel distance for implicitly modelled avalanches is 1500 m, which is generous when compared to the findings of Butler and Malanson (1992), D. K. Singh et al. (2020), and Teich et al. (2012). A more conservative maximum travel distance would dampen the occurrence of unnaturally large areas of classified avalanche deposits.

More snow removal was attributed to avalanching than to wind in terms of SCA. However, a trial inspection of satellite images (e.g., October 27-28, 2020, Figure 10) revealed no scarps, break lines, lobes or other evidence of avalanches. This indicates that SRCM's ASI threshold of 6.69 was too low, implying that the Jenks classification method resulted in unnaturally large high-susceptibility areas. Alternative classification methods could result in differently distributed ASI classes and a higher ASI threshold. For example, an equal interval classification or setting the threshold to 2 standard deviations above the mean would have yielded ASI thresholds of 7.11 or 7.75, respectively. Alternatively, the ASI could be categorized into more than four classes, also increasing the threshold for the highest-susceptibility class. These solutions would exercise less weight on SRCM's avalanching classification scheme, resulting in more balanced classification mechanisms.

Moreover, the overclassification of snow removal by avalanching is partly caused by the MCDA-AHP method used to compute the ASI. As Equation 2 does not include snow depth, but only snow cover, it implies that avalanches can form in very thin snowpacks. This leads to unrealistically large areas of classified avalanche source areas. Thus, consideration of snow depths is important for improving the accuracy of avalanche classifications.

5.3.3 Sublimation

The PlanetScope scenes of October 27 and 28, 2020, in Figure 10 are mostly cloud-free, meaning that solar radiation could have contributed to the snow ablation process by causing sublimation. As radiative transfer processes like sensible and latent heat fluxes are not implemented in SPHY, the sublimation of

snow is not accounted for. This is problematic, as sublimation can account for up to 21% of annual snowfall in the Himalaya and possibly more at wind-exposed locations (Stigter et al., 2018).

Sublimation is neither explicitly accounted for in SRCM, although one could argue that it is implicitly. Whereas snow sublimation can take place from the ground or from vegetation canopies, the majority (4-10 times as much in terms of SWE) of sublimation takes place from turbulent suspension (Strasser et al., 2008). This means that the snow sublimates *after* entrainment by the wind. As this study focused primarily on wind-driven removal of snow cover from the ground, which occurs *before* sublimation, the effects of the process were considered negligible for this study. Furthermore, sublimation may account for a fraction of SWE loss, but it is unlikely to completely remove the snow cover. If the snow cover depletes, the albedo decreases and more solar radiation is transferred to sensible heat at the expense of latent heat, which then stimulates melting instead of sublimation.

5.3.4 Eolian snow redistribution

The seasonal variability of the threshold wind speed for blowing snow, visible in the 2020 panel of Figure 11, is most likely related to the age and wetness of the snowpack. Fresh or dry snow requires lower wind speeds to be blown away than aged or wet snow (Li & Pomeroy, 1997). This is because wet snow has larger intergranular cohesive forces, that require larger opposing forces (i.e. higher wind speeds) to break the cohesive bonds and allow for the entrainment of snow particles (Schmidt, 1980). Aged snow also requires a higher threshold wind speed, because increasing snowpack age allows for more compaction, crystal restructuring and metamorphosis to occur, thereby increasing the force required to release snow particles from the snowpack.

From December until March, average temperatures are below freezing and precipitation falls as snow, resulting in fresh and dry snowpacks. From April until July, temperatures increase, leading to reduced snowfall and increased rainfall and snowmelt, resulting in the aging and wetting of the remaining snow. This trend continues throughout the monsoon season, thereby increasing the wind speed required for snow transport. Threshold wind speed ranges for the transport of wet and dry snow have been previously established in the literature (Li & Pomeroy, 1997). Specifically, these are 7-14 m/s for wet snow and 4-11 m/s for dry snow. Figure 11 shows that in 2020, the wind speed ranges at which the snow removal frequencies are highest (>0.9, where points are most red) agree with the established threshold range for dry snow from December until April and with the range for wet snow from May until November.

For the deposition of wind-supplied snow, the frequency decreases with decreasing wind speed below the threshold (Figure 12). Snow particles only remain suspended in the wind for as long as the wind speed is above the threshold. If the required wind speed is not sustained, the particles will be deposited. As the threshold in SRCM is set to 4 m/s (after Li and Pomeroy (1997)), any wind speeds just below this result in the immediate deposition of snow. This is apparent in Figure 12, as high deposition frequencies (>0.9) occur over 1.5 times as often at wind speeds of 2.5-4.0 m/s than at speeds of 0.0-2.5 m/s.

A distinction can be made between static and dynamic thresholds (Bagnold, 1941). The former describes the wind speed necessary to initiate particle motion and the latter describes the lowest wind speed at which particle motion can be sustained. For wind-driven transport of non-cohesive particles, the dynamic threshold is generally 0.8 times the static threshold (Greeley & Iversen, 1987). This is because once they drop out of suspension, the kinetic energy of saltating particles provides impact forces that dislodge stationary particles (Schmidt, 1980). Based on this distinction, one could argue that the (dynamic) threshold for the deposition of snow is lower than the (static) threshold for the removal of snow. However, snow particles *are* cohesive, to such an extent that shear forces exerted by wind are insufficient to initiate particle transport (Schmidt, 1980). Thus, snow particles require impact forces to be ejected from the surface, rendering the static threshold unsuitable for snow. Hence, snow transport requires a dynamic threshold that applies to both removal and deposition. Recently, a new formula was established for calculating this threshold wind speed using snow temperature, particle size and deposition time (He & Ohara, 2017), but these data were not available for the study area.

5.4 Interpretation of snow redistribution patterns

5.4.1 Spatial heterogeneity and subgrid variability

The wind-driven snow removal and deposition patterns displayed in Figure 14 and Figure 15 correspond well to the prevailing wind directions (Figure 4) and the topographic exposure in those directions (Figure 6). The contrast between the concentrated wind-driven snow removal areas and the widespread wind-supplied snow deposition areas illustrates the dispersivity of the snow redistribution process. Eolian snow removal is very spatially heterogeneous because high wind speeds often occur in very short-lived, local gusts (Ágústsson & Ólafsson, 2004). Snow that is entrained by these gusts disperses in turbulent suspension before being deposited over a larger area at lower wind speeds. Likewise, the short lifespan of wind gusts (several seconds) allows entrained snow to only travel a limited distance, often depositing it in a more sheltered area. Thus, the amount of deposition of wind-supplied snow is inversely proportional to the distance from the source area. This pattern is especially well-established in the December panel of Figure 15. These findings support those of Bernhardt et al. (2012), Dadic et al. (2010), Hiemstra et al. (2002), Liston and Sturm (1998), Mott and Lehning (2010), and Pomeroy et al. (1998).

The effect of trees on snow redistribution is limited to scales of ca. 5 m and superimposed onto the topographical effects on snow redistribution (Hiemstra et al., 2002). Despite forests covering roughly half of Din-Gad Catchment, these effects are not considered in this study. WindNinja does require vegetation type as input but assumes it to be homogeneous across the entire domain. Hence, the downscaled wind fields and modelled snow redistribution patterns are probably more accurate in the non-vegetated parts of the study domain. Furthermore, this study does not consider eolian snow redistribution patterns at scales below 30 m. This means that small-scale snow deposition patterns such as dunes and cornices cannot be identified. These require wind and snow transport models at resolutions below 10 m to be identified (Mott & Lehning, 2010).

5.4.2 Implications for hydrological modelling

Eolian snow redistribution has been shown to increase snow cover heterogeneity compared to TI-based snow cover simulations (Bernhardt et al., 2010a; Liston, 2004; Mott & Lehning, 2010). At which scales this affects the hydrological behaviour of snowmelt runoff depends on whether there is a net influx or outflux of snow from the catchment. The significantly higher number of snow deposition cells versus snow removal cells indicates a net increase in SCA over the 2017-2020 period. However, this does not necessarily mean that the amount of snow in Din-Gad Catchment has increased, as snow depths remain unknown. It is more likely that snow from thick snowpacks (e.g., accumulated snow on ridges) was dispersed and spread over larger, snow-free areas, increasing the SCA in the catchment.

As discussed briefly in Section 5.3.1, SC change occurs at modest snow depths. The scope of this study is restricted to snow cover due to the absence of snow depth data. The incorporation of snow depths into the methodology would greatly benefit the accuracy of the snow redistribution classifications. The extra dimension would facilitate the modelling of changes in snow storage, as apposed to snow cover. This would enable quantification of snow redistribution volumes, which are valuable hydrological insights. The spatial distribution of snow determines that of snowmelt runoff (Brauchli et al., 2017). Thin snowpacks result in fast melting and runoff generation, as they require relatively little energy to melt and the generated meltwater must only travel a limited distance. Contrarily, large snow accumulations require more energy to melt, resulting in slower melting and delayed runoff generation, as the meltwater must travel a greater distance. Thus, the snow redistribution not only alters the spatial component of hydrologic behaviour, but also the timing and duration of snowmelt runoff. This emphasizes the importance of including snow redistribution processes in hydrological models, especially in high-mountain areas (Brauchli et al., 2017).

5.5 Limitations of this study

The method used in this study has three main limitations, which are all inherent to the use of optical satellite imagery. Firstly, the spatiotemporal availability of data is limited by satellite specifications and cloud cover. Few Earth observation platforms provide daily, high-resolution, global coverage and even fewer are publicly accessible. Clouds create an unavoidable issue when working with passive optical sensors, often severely limiting the spatial coverage of the study domain. Secondly, optical imagery can only be used for studying binary snow cover, but not for snow depth or snow storage. This is fundamentally restrictive for studying snow redistribution volumes. Lastly, validation of the results is impossible without ground truth data, whether they are field observations or AWS measurements. The highest degree of evaluation in this study is achieved by comparing the SRCM results to the satellite images of the same day.

The data used in this study also bear limitations. For example, the majority of the satellite imagery was sourced from the PlanetScope platform (Figure 2), which is not equipped with a SWIR sensor. Instead of deriving snow cover from the NDSI, which is computed using the SWIR band, SC from PlanetScope

imagery was derived using the pre-classified UDM2 band, which is less accurate. To circumvent this issue, preference was given to Sentinel-2 and Landsat 8 imagery where possible. For these platforms, a constant NDSI value of 0.2 was used to distinguish between snow-covered and snow-free ground. The effectiveness of this threshold depends on the brightness of a scene (which is related to the solar zenith angle and atmospheric conditions) and whether a pixel is located in a shadow (terrain shadow or cloud shadow) and thus performs differently per pixel (Kour et al., 2016). A spatiotemporally variable NDSI threshold is likely to produce more accurate SC maps, but proper calibration of the appropriate threshold ranges requires seasonal in situ measurements like ground-based photographs (Härer et al., 2016; Härer et al., 2018). The empirically-derived NDSI threshold of 0.2 was based on the year-round characteristic bimodal distribution of the NDSI values for both satellite platforms. Whilst this makes the threshold quite temporally robust, the spatial errors caused by shadows are not considered. SCA is often underestimated in shadow areas (Jasrotia et al., 2022), highlighting a probable cause of the 61.6% of unexplained SC changes by SRCM. A spatially variable NDSI threshold, that accounts for the effects of shadows, would lead to a higher overall classification ratio for SRCM.

Regarding the interpretation of snow redistribution patterns, care must be taken when inferring the source areas of snow deposits. When snow is *removed* by wind, the travel direction can be inferred from the wind direction. However, the wind direction in a snow *deposition* cell does not necessarily provide accurate information on the direction of origin of the snow. Essentially, the wind may follow a non-straight flow path and continue for an unknown duration. Ultimately, approximating the source area of a wind-supplied snow deposit is only possible using wind duration data. Long, strong winds may cause more frequent wind-induced snow removal and more distal snow deposits, potentially resulting in a net influx or outflux of snow from the catchment. ERA5-Land provides hourly wind data, which could be used to create downscaled hourly wind fields. Even so, the computational demand would be unreasonably high and no existing satellite platform provides hourly imagery with global coverage, so any modelled snow redistribution at a sub-daily time scale could not be evaluated. In fact, pinpointing the exact source area of eolian snow deposits and evaluating sub-daily wind and snow dynamics requires a fully distributed dynamic atmospheric model with advanced particle backtracking.

5.6   Implications and recommendations

The study of Bernhardt et al. (2012) provided valuable insights into the effects of gravitational and eolian snow redistribution on snow melt and sublimation. In an attempt to deepen this knowledge, these effects have been studied in a more topographically extreme area. Although this study takes a more empirical approach, rather than the physically-based modelling approach of Bernhardt et al. (2012), the general findings regarding the snow redistribution patterns agree. However, their findings on hydrological effects, like reduced snowmelt on crests and increased snowmelt at foothills, due to redistribution of snow from exposed to sheltered locations, cannot be supported by this study due to the absence of snow depth data.

An alternative approach to studying snow redistribution is by using a Snow Persistence (SP) index as a proxy indicator. SP is a simple metric of snow cover duration that describes the normalized snow cover duration, i.e. the number of snow-covered days over the total number of days in a certain period. SP has been proven to be an appropriate metric for tracking SC changes (Nolin et al., 2021) and a potential descriptor and predictor of hydrological behaviour (Le et al., 2022). Its advantages are that no meteorological data are required and it can be easily derived using satellite imagery (Hammond et al., 2018).

Wayand et al. (2018) have studied large-scale snow redistribution in the Canadian Rocky Mountains. They identified 7979 ridges in a study area of 21,118 km^2, over which they analysed trends of SP, shortwave irradiance and elevation perpendicular to the ridges. Their statistical approach reasoned that when the SP and shortwave irradiance profiles showed a strong negative correlation, the snow distribution patterns were largely determined by melting. When the correlation was different, the patterns were attributed to the redistribution of snow by wind or gravity, making no distinction between the two. This approach is limited to indirectly quantifying one-dimensional snow redistribution over different ridge types and is only suitable for mapping large-scale redistribution patterns on monthly to yearly time scales. One month's worth of daily imagery is just enough to compute a reliable SP index, making sub-monthly analysis difficult. Also, only large study areas (ca. >1000 km^2) will provide enough ridges and topographic features from which to derive reliable statistics.

As the current study domain is only 207 km^2 and the main interest was identifying two-dimensional snow redistribution patterns, a different approach was used for this study. Most importantly, this included an attempt to distinctly classify avalanches and wind-driven snow redistribution and the evaluation of patterns using downscaled wind fields, all on a near-daily basis. For study areas up to 2500 km^2 (based on the computational limitations of WindNinja), a combination of methods from both studies could yield better insights into snow redistribution and bridge the gap between small-scale and large-scale analysis in both the spatial and temporal domains.

Based on this study, a few recommendations can be made for future research. Firstly, the use of radar imagery provides numerous advantages over optical imagery. These include (1) better spatial coverage, as clouds do not obstruct the view of active Synthetic Aperture Radar (SAR) sensors, (2) the support of snow depth measurements and (3) the possibility of distinguishing between wet and dry snow (Buchelt et al., 2022; Marin et al., 2020; Nagler et al., 2016). This would enable the quantification of snow redistribution volumes and evaluation of variable threshold wind speeds for the transport of wet and dry snow. The Sentinel-1 platform is exceptionally suitable for this application and is also accessible through the Google Earth Engine data catalog (Gorelick et al., 2017).

Secondly, it is appropriate to conduct sensitivity analysis and error propagation tests when working with an empirical classification model like SRCM. This way, the effects of thresholds like the NDSI, ASI or wind speed for snow transport can be investigated. Also, the extent to which any assumptions affect the final results can be quantified. Ultimately, this will increase the SC change classification ratio.

Lastly, it is recommended to include field observations where possible. The incorporation of ground truth data, whether it is field data or AWS measurements, enables the calibration of the models that constitute the methodology. This allows the results to be validated, fundamentally increasing the accuracy of simulations and classifications.

6 Conclusion

This study aims to identify eolian snow redistribution patterns in Din-Gad Catchment, Central Himalaya. This was done using an unprecedented combination of optical satellite imagery (Sentinel-2, Landsat 8 and PlanetScope), climate reanalysis data (ERA5, ERA5-Land), downscaled wind fields (WindNinja), a TI-based hydrological model (SPHY) and a newly developed empirical classification model for snow redistribution mechanisms (SRCM). Snow cover changes from January 1, 2017, to December 31, 2020, were identified and attributed to three different snow removal and deposition mechanisms on a near-daily basis. The results were aggregated per month to assess the eolian snow redistribution patterns.

The results show that of all snow cover changes, SRCM classified 21.6% as wind-driven and 14.1% as gravity-driven. Remarkably, almost 1.6 times as much snow removal was attributed to avalanching than to wind-driven removal, whereas wind-supplied snow deposition was classified almost 4.7 times as frequently as deposition by avalanching. Evaluation of SRCM's performance by inspection of satellite images revealed that large areas were misinterpreted as avalanche source areas or deposits. Also, large areas of snow cover change on either side of the snow line were incompletely simulated by SPHY using the model parameters specific to this study.

The eolian snow redistribution patterns corresponded well with the topographic exposure and prevailing wind directions. Wind-induced snow removal was most frequent in areas that are topographically exposed in the wind direction and wind-supplied snow deposition was most frequent in topographically sheltered areas. Low domain-averaged maximum wind speeds resulted in concentrated snow ablation zones, whereas eolian snow deposition was generally widespread across the valleys and lee sides of topographic obstacles. The threshold wind speed for snow transport seems seasonally variable, starting low in winter and increasing during the monsoon months. This temporal shift is likely caused by the changing age and wetness of the snowpack, as wind speeds drop, temperatures rise and precipitation increases during the onset of the monsoon season. The monthly wind-driven snow redistribution patterns reflect the changes in prevailing wind speed and direction and illustrate the dispersive nature of turbulent snow transport.

Regarding avalanches, the approximation of source and deposition areas using assumptions about watershed, elevation and maximum travel distance yields insufficient results. More accurate classification of avalanche areas requires consideration of snow depth, flow direction and flow accumulation data. Likewise, the simple parameterization of temperature lapse rate in SPHY is inadequate for modelling snow cover evolution in the complex terrain of Din-Gad Catchment. With the chosen model parameters,

SPHY showed difficulty observing snow cover changes based on temperature and precipitation alone, suggesting that it would greatly benefit from the development of an additional module that accounts for snow redistribution processes. However, exact quantification of how much snow cover change is overlooked requires more extensive research using different model parameters.

Optical satellite imagery and wind fields from downscaled climate reanalysis data are suitable for deriving eolian snow redistribution patterns in extreme topography up to a spatiotemporal resolution of 30 m near-daily. The accuracy of the results is limited by cloud cover, the absence of a SWIR band and field observations and the robustness of model assumptions. These limitations can be overcome by including radar imagery and AWS data, incorporating a spatiotemporally variable NDSI threshold and performing sensitivity analyses on model threshold parameters. Combining this with a snow persistence index, data on solar radiation and the methods and findings of this study could provide a promising basis for future research on eolian snow redistribution. This research is relevant to understanding the snow dynamics in high-mountain areas and provides insights that contribute to the improvement of hydrological models.

Acknowledgements

Data availability

The data and scripts used in this study are available on Zenodo (https://doi.org/10.5281/zenodo.7861614). This includes the pre-processed satellite imagery, downscaled wind fields, SPHY reference data, SRCM python model and its raw and aggregated outputs. The Google Earth Engine script for pre-processing the satellite imagery is available via https://code.earthengine.google.com/b7fe3ca48de410c9a3fff842f88a1e7f. The data is available for academic research purposes only. Any use of the data should acknowledge the author and this thesis as the legitimate source. For any questions or requests related to the data, please contact the author, L.R. van Dijk, at lucvandijk@quicknet.nl.

References

Acharki, S. (2022). PlanetScope contributions compared to Sentinel-2, and Landsat-8 for LULC mapping. *Remote Sensing Applications: Society and Environment*, *27*. https://doi.org/10.1016/j.rsase.2022.100774

Ágústsson, H., & Ólafsson, H. (2004). Mean gust factors in complex terrain. *Meteorologische Zeitschrift*, *13*, 149–155. https://doi.org/10.1127/0941-2948/2004/0013-0149

Armstrong, R. L., Rittger, K., Brodzik, M. J., Racoviteanu, A., Barrett, A. P., Khalsa, S. J. S., Raup, B., Hill, A. F., Khan, A. L., Wilson, A. M., Kayastha, R. B., Fetterer, F., & Armstrong, B. (2019). Runoff from glacier ice and seasonal snow in High Asia: separating melt water sources in river flow. *Regional Environmental Change*, *19*, 1249–1261. https://doi.org/10.1007/s10113-018-1429-0

Bagnold, R. A. (1941). *The Physics of Blown Sand and Desert Dunes*. Chapman & Hall.

Balk, B., & Elder, K. (2000). Combining binary decision tree and geostatistical methods to estimate snow distribution in a mountain watershed. *Water Resources Research*, *36*, 13–26. https://doi.org/10.1029/1999WR900251

Barnett, T. P., Adam, J. C., & Lettenmaier, D. P. (2005). Potential impacts of a warming climate on water availability in snow-dominated regions. *Nature*, *438*, 303–309. https://doi.org/10.1038/nature04141

Beniston, M., & Stoffel, M. (2014). Assessing the impacts of climatic change on mountain water resources. *Science of the Total Environment*, *493*, 1129–1137. https://doi.org/10.1016/j.scitotenv.2013.11.122

Bernhardt, M., Liston, G. E., Strasser, U., Zängl, G., & Schulz, K. (2010a). High resolution modelling of snow transport in complex terrain using downscaled MM5 wind fields. *The Cryosphere*, *4*, 99–113. www.the-cryosphere.net/4/99/2010/

Bernhardt, M., & Schulz, K. (2010b). SnowSlide: A simple routine for calculating gravitational snow transport. *Geophysical Research Letters*, *37*. https://doi.org/10.1029/2010GL043086

Bernhardt, M., Schulz, K., Liston, G. E., & Zängl, G. (2012). The influence of lateral snow redistribution processes on snow melt and sublimation in alpine regions. *Journal of Hydrology*, *424-425*, 196–206. https://doi.org/10.1016/j.jhydrol.2012.01.001

Bernhardt, M., Zängl, G., Liston, G. E., Strasser, U., & Mauser, W. (2009). Using wind fields from a high-resolution atmospheric model for simulating snow dynamics in mountainous terrain. *Hydrological Processes*, *23*, 1064–1075. https://doi.org/10.1002/hyp.7208

Biemans, H., Siderius, C., Lutz, A. F., Nepal, S., Ahmad, B., Hassan, T., von Bloh, W., Wijngaard, R. R., Wester, P., Shrestha, A. B., & Immerzeel, W. W. (2019). Importance of snow and glacier meltwater for agriculture on the Indo-Gangetic Plain. *Nature Sustainability*, *2*, 594–601. https://doi.org/10.1038/s41893-019-0305-3

Bormann, K. J., Brown, R. D., Derksen, C., & Painter, T. H. (2018). Estimating snow-cover trends from space. *Nature Climate Change*, *8*, 924–928. https://doi.org/10.1038/s41558-018-0318-3

Bowen, A. J., & Lindley, D. (1974). Measurements of the mean wind flow over various escarpment shapes. *Proceedings of the Fifth Australasian Conference on Hydraulics and Fluid Mechanics*, 211–219.

Bowling, L. C., Pomeroy, J. W., & Lettenmaier, D. P. (2004). Parameterization of blowing-snow sublimation in a macroscale hydrology model. *Journal of Hydrometeorology*, *5*, 745–762.

Brauchli, T., Trujillo, E., Huwald, H., & Lehning, M. (2017). Influence of slope-scale snowmelt on catchment response simulated with the Alpine3D model. *Water Resources Research*, *53*, 10723–10739. https://doi.org/10.1002/2017WR021278

Buchelt, S., Skov, K., Rasmussen, K. K., & Ullmann, T. (2022). Sentinel-1 time series for mapping snow cover depletion and timing of snowmelt in Arctic periglacial environments: Case study from Zackenberg and Kobbefjord, Greenland. *Cryosphere*, *16*, 625–646. https://doi.org/10.5194/tc-16-625-2022

Buchhorn, M., Lesiv, M., Tsendbazar, N. E., Herold, M., Bertels, L., & Smets, B. (2020). Copernicus global land cover layers - collection 2. *Remote Sensing*, *12*. https://doi.org/10.3390/rs12061044

Butler, D. R., & Malanson, G. P. (1992). Effects of terrain on excessive travel distance by snow avalanches. *Northwest Science*, *66*(2).

Chauhan, M. (2010). A perspective on watershed development in the Central Himalayan state of Uttarakhand, India. *International Journal of Ecology and Environmental Sciences*, *36*, 253–269.

Cullen, N. J., Steffen, K., & Blanken, P. D. (2007). Nonstationarity of turbulent heat fluxes at Summit, Greenland. *Boundary-Layer Meteorology*, *122*, 439–455. https://doi.org/10.1007/s10546-006-9112-2

Dadic, R., Mott, R., Lehning, M., & Burlando, P. (2010). Wind influence on snow depth distribution and accumulation over glaciers. *Journal of Geophysical Research: Earth Surface*, *115*. https://doi.org/10.1029/2009JF001261

Déry, S. J., & Yau, M. K. (1999). A bulk blowing snow model. *Boundary-Layer Meteorology*, *93*, 237–251.

Dimri, T., Ahmad, S., & Sharif, M. (2022). Statistical analysis of precipitation, temperature and snow cover in Bhagirathi River basin. *Mausam*, *73*, 263–272. https://doi.org/10.54302/mausam.v73i2.5477

Dozier, J., Bair, E. H., & Davis, R. E. (2016). Estimating the spatial distribution of snow water equivalent in the world's mountains. *Wiley Interdisciplinary Reviews: Water*, *3*, 461–474. https://doi.org/10.1002/wat2.1140

Eidsvik, K. J., Holstad, A., Lie, I., & Utnes, T. (2004). A prediction system for local wind variations in mountainous terrain. *Boundary-Layer Meteorology*, *112*, 557–586.

Essery, R. (2001). Spatial statistics of windflow and blowing-snow fluxes over complex topography. *Boundary-Layer Meteorology*, *100*, 131–147.

Essery, R., Li, L., & Pomeroy, J. (1999). A distributed model of blowing snow over complex terrain. *Hydrological Processes*, *13*, 2423–2438.

Farr, T. G., Rosen, P. A., Caro, E., Crippen, R., Duren, R., Hensley, S., Kobrick, M., Paller, M., Rodriguez, E., Roth, L., Seal, D., Shaffer, S., Shimada, J., Umland, J., Werner, M., Oskin, M., Burbank, D., & Alsdorf, D. E. (2007). The Shuttle Radar Topography Mission. *Reviews of Geophysics*, *45*. https://doi.org/10.1029/2005RG000183

Fiddes, J., & Gruber, S. (2014). TopoSCALE v.1.0: Downscaling gridded climate data in complex terrain. *Geoscientific Model Development*, *7*, 387–405. https://doi.org/10.5194/gmd-7-387-2014

Forthofer, J. M., Butler, B. W., & Wagenbrenner, N. S. (2014). A comparison of three approaches for simulating fine-scale surface winds in support of wildland fire management. Part I. Model formulation and comparison against measurements. *International Journal of Wildland Fire*, *23*, 969–981. https://doi.org/10.1071/WF12089

Freudiger, D., Kohn, I., Seibert, J., Stahl, K., & Weiler, M. (2017). Snow redistribution for the hydrological modeling of alpine catchments. *Wiley Interdisciplinary Reviews: Water*, *4*(5).

Friedl, M., & Sulla-Menashe, D. (2022). *MODIS/Terra+Aqua Land Cover Type Yearly L3 Global 500m SIN Grid V061 MCD12Q1.061* [Accessed on March 6, 2023]. NASA EOSDIS Land Processes DAAC. https://doi.org/10.5067/MODIS/MCD12Q1.061

Gorelick, N., Hancher, M., Dixon, M., Ilyushchenko, S., Thau, D., & Moore, R. (2017). Google Earth Engine: Planetary-scale geospatial analysis for everyone. *Remote Sensing of Environment*, *202*, 18–27. https://doi.org/10.1016/j.rse.2017.06.031

Gourav, P., Kumar, R., Gupta, A., & Arif, M. (2020). Flood hazard zonation of Bhagirathi River basin using multi-criteria decision-analysis in Uttarakhand, India. *International Journal on Emerging Technologies*, *11*, 62–71. https://www.researchgate.net/publication/338526972

Greeley, R., & Iversen, J. D. (1987). *Wind as a geological process: on Earth, Mars, Venus and Titan*. CUP Archive.

Hall, D. K., & Riggs, G. A. (2010). Normalized-Difference Snow Index (NDSI). *Encyclopedia of Snow, Ice and Glaciers*.

Hammond, J. C., Saavedra, F. A., & Kampf, S. K. (2018). Global snow zone maps and trends in snow persistence 2001–2016. *International Journal of Climatology*, *38*, 4369–4383. https://doi.org/10.1002/joc.5674

Härer, S., Bernhardt, M., & Schulz, K. (2016). PRACTISE - Photo Rectification and ClassificaTIon SoftwarE (V.2.1). *Geoscientific Model Development*, *9*, 307–321. https://doi.org/10.5194/gmd-9-307-2016

Härer, S., Bernhardt, M., Siebers, M., & Schulz, K. (2018). On the need of a time- and location-dependent estimation of the NDSI threshold value for reducing existing uncertainties in snow cover maps at different scales. *Cryosphere*, *12*, 1629–1642. https://doi.org/10.5194/tc-2017-177

He, S., & Ohara, N. (2017). A new formula for estimating the threshold wind speed for snow movement. *Journal of Advances in Modeling Earth Systems*, *9*, 2514–2525. https://doi.org/10.1002/2017MS000982

Hersbach, H., Bell, B., Berrisford, P., Hirahara, S., Horányi, A., Muñoz-Sabater, J., Nicolas, J., Peubey, C., Radu, R., Schepers, D., Simmons, A., Soci, C., Abdalla, S., Abellan, X., Balsamo, G., Bechtold, P., Biavati, G., Bidlot, J., Bonavita, M., . . . Thépaut, J. N. (2020). The ERA5 global reanalysis. *Quarterly Journal of the Royal Meteorological Society*, *146*, 1999–2049. https://doi.org/10.1002/qj.3803

Hiemstra, C. A., Liston, G. E., & Reiners, W. A. (2002). Snow redistribution by wind and interactions with vegetation at upper treeline in the Medicine Bow Mountains, Wyoming, U.S.A. *Arctic, Antarctic, and Alpine Research*, *34*, 262–273. https://doi.org/10.1080/15230430.2002.12003493

Hock, R. (2003). Temperature index melt modelling in mountain areas. *Journal of Hydrology*, *282*, 104–115. https://doi.org/10.1016/S0022-1694(03)00257-9

Huss, M., Bookhagen, B., Huggel, C., Jacobsen, D., Bradley, R. S., Clague, J. J., Vuille, M., Buytaert, W., Cayan, D. R., Greenwood, G., Mark, B. G., Milner, A. M., Weingartner, R., & Winder, M. (2017). Toward mountains without permanent snow and ice. *Earth's Future*, *5*, 418–435. https://doi.org/10.1002/2016EF000514

Huss, M., & Hock, R. (2018). Global-scale hydrological response to future glacier mass loss. *Nature Climate Change*, *8*, 135–140. https://doi.org/10.1038/s41558-017-0049-x

Immerzeel, W. W., & Bierkens, M. F. (2012). Asia's water balance. *Nature Geoscience*, *5*, 841–842. https://doi.org/10.1038/ngeo1643

Immerzeel, W. W., Lutz, A. F., Andrade, M., Bahl, A., Biemans, H., Bolch, T., Hyde, S., Brumby, S., Davies, B. J., Elmore, A. C., Emmer, A., Feng, M., Fernández, A., Haritashya, U., Kargel, J. S., Koppes, M., Kraaijenbrink, P. D., Kulkarni, A. V., Mayewski, P. A., . . . Baillie, J. E. (2020). Importance and vulnerability of the world's water towers. *Nature*, *577*, 364–369. https://doi.org/10.1038/s41586-019-1822-y

Immerzeel, W. W., Beek, L. P. H. V., & Bierkens, M. F. P. (2010). Climate change will affect the Asian water towers. *Science*, *328*, 1382–1385. https://doi.org/10.1126/science.1183188

Jasrotia, A. S., Kour, R., & Singh, K. K. (2022). Effect of shadow on atmospheric and topographic processed NDSI values in Chenab basin, Western Himalayas. *Cold Regions Science and Technology*, *199*. https://doi.org/10.1016/j.coldregions.2022.103561

Jenks, G. F. (1967). The data model concept in statistical mapping. *International yearbook of cartography*, *7*, 186–190.

Jiang, H., & Eastman, J. R. (2000). Application of fuzzy measures in multi-criteria evaluation in GIS. *International Journal of Geographical Information Science*, *14*, 173–184. https://doi.org/10.1080/136588100240903

Joshi, R., Kumar, K., Pandit, J., & Palni, L. M. S. (2015). Variations in the Seasonal Snow Cover Area (SCA) for Upper Bhagirathi Basin, India. *Dynamics of Climate Change and Water Resources of Northwestern Himalaya*, 9–21. https://doi.org/10.1007/978-3-319-13743-8_2

Kapnick, S. B., Delworth, T. L., Ashfaq, M., Malyshev, S., & Milly, P. C. (2014). Snowfall less sensitive to warming in Karakoram than in Himalayas due to a unique seasonal cycle. *Nature Geoscience*, *7*, 834–840. https://doi.org/10.1038/ngeo2269

Karssenberg, D., Schmitz, O., Salamon, P., de Jong, K., & Bierkens, M. F. (2010). A software framework for construction of process-based stochastic spatio-temporal models and data assimilation. *Environmental Modelling and Software*, *25*, 489–502. https://doi.org/10.1016/j.envsoft.2009.10.004

Kattel, D. B., Yao, T., Yang, K., Tian, L., Yang, G., & Joswiak, D. (2013). Temperature lapse rate in complex mountain terrain on the southern slope of the Central Himalayas. *Theoretical and Applied Climatology*, *113*, 671–682. https://doi.org/10.1007/s00704-012-0816-6

Keenan, E., Wever, N., Lenaerts, J. T. M., & Medley, B. (2022). A wind-driven snow redistribution module for Alpine3D v3.3.0: Adaptations designed for downscaling ice sheet surface mass balance. *Geoscientific Model Development Discussions*, 1–24. https://doi.org/10.5194/gmd-2022-28

Khanal, S., Lutz, A. F., Kraaijenbrink, P. D., van den Hurk, B., Yao, T., & Immerzeel, W. W. (2021). Variable 21st century climate change response for rivers in High Mountain Asia at seasonal to decadal time scales. *Water Resources Research*, *57*. https://doi.org/10.1029/2020WR029266

Khanal, S., Nick, F. M., Fiddes, J., Kraaijenbrink, P. D. A., & Immerzeel, W. W. (In Review). *Present-day and future changes in the hydrology of the Bhagirathi Basin* (Report 244). FutureWater. https://www.futurewater.eu/publications/

Kour, R., Patel, N., & Krishna, A. P. (2016). Influence of shadow on the thermal and optical snow indices and their interrelationship. *Remote Sensing of Environment*, *187*, 119–129. https://doi.org/10.1016/j.rse.2016.10.017

Kraaijenbrink, P. D., Bierkens, M. F., Lutz, A. F., & Immerzeel, W. W. (2017). Impact of a global temperature rise of 1.5 degrees Celsius on Asia's glaciers. *Nature*, *549*, 257–260. https://doi.org/10.1038/nature23878

Kraaijenbrink, P. D., Stigter, E. E., Yao, T., & Immerzeel, W. W. (2021). Climate change decisive for Asia's snow meltwater supply. *Nature Climate Change*, *11*, 591–597. https://doi.org/10.1038/s41558-021-01074-x

Kumar, S., Srivastava, P. K., & Snehmani. (2017). GIS-based MCDA–AHP modelling for avalanche susceptibility mapping of Nubra valley region, Indian Himalaya. *Geocarto International*, *32*, 1254–1267. https://doi.org/10.1080/10106049.2016.1206626

Le, E., Ameli, A. A., Janssen, J., & Hammond, J. (2022). Snow persistence explains stream high flow and low flow signatures with differing relationships by aridity and climatic seasonality. *Hydrology and Earth System Sciences*. https://doi.org/10.5194/hess-2022-106

Lehning, M., Ingo, I. V., Gustafsson, D., Nguyen, T. A., Stähli, M., & Zappa, M. (2006). ALPINE3D: A detailed model of mountain surface processes and its application to snow hydrology. *Hydrological Processes*, *20*, 2111–2128. https://doi.org/10.1002/hyp.6204

Li, L., & Pomeroy, J. W. (1997). Estimates of threshold wind speeds for snow transport using meteorological data. *Journal of Applied Meteorology*, *36*, 205–213.

Liston, G. E. (1995). Local advection of momentum, heat and moisture during the melt of patchy snow covers. *Journal of Applied Meteorology*, *34*, 1705–1715.

Liston, G. E. (2004). Representing subgrid snow cover heterogeneities in regional and global models. *Journal of Climate*, *17*, 1381–1397.

Liston, G. E., & Elder, K. (2006). A distributed snow-evolution modeling system (SnowModel). *Journal of Hydrometeorology*, *7*, 1259–1276.

Liston, G. E., & Sturm, M. (1998). A snow-transport model for complex terrain. *Journal of Glaciology*, *44*, 498–516. https://doi.org/10.3189/s0022143000002021

Livneh, B., & Badger, A. M. (2020). Drought less predictable under declining future snowpack. *Nature Climate Change*, *10*, 452–458. https://doi.org/10.1038/s41558-020-0754-8

Lobeto, H., Menendez, M., Losada, I. J., & Hemer, M. (2022). The effect of climate change on wind-wave directional spectra. *Global and Planetary Change*, *213*. https://doi.org/10.1016/j.gloplacha.2022.103820

Lutz, A. F., Immerzeel, W. W., Shrestha, A. B., & Bierkens, M. F. (2014a). Consistent increase in High Asia's runoff due to increasing glacier melt and precipitation. *Nature Climate Change*, *4*, 587–592. https://doi.org/10.1038/nclimate2237

Mallare, R. A., Shintani, T., & Yokoyama, K. (2022). Estimation of non-uniform wind field over a meandering reservoir. *Journal of Japan Society of Civil Engineers, Ser. B1 (Hydraulic Engineering)*, *78*(2), I_1039–I_1044.

Mankin, J. S., Viviroli, D., Singh, D., Hoekstra, A. Y., & Diffenbaugh, N. S. (2015). The potential for snow to supply human water demand in the present and future. *Environmental Research Letters*, *10*. https://doi.org/10.1088/1748-9326/10/11/114016

Marin, C., Bertoldi, G., Premier, V., Callegari, M., Brida, C., Hürkamp, K., Tschiersch, J., Zebisch, M., & Notarnicola, C. (2020). Use of Sentinel-1 radar observations to evaluate snowmelt dynamics in alpine regions. *Cryosphere*, *14*, 935–956. https://doi.org/10.5194/tc-14-935-2020

Mott, R., & Lehning, M. (2010). Meteorological modeling of very high-resolution wind fields and snow deposition for mountains. *Journal of Hydrometeorology*, *11*, 934–949. https://doi.org/10.1175/2010JHM1216.1

Muñoz-Sabater, J., Dutra, E., Agustí-Panareda, A., Albergel, C., Arduini, G., Balsamo, G., Boussetta, S., Choulga, M., Harrigan, S., Hersbach, H., Martens, B., Miralles, D. G., Piles, M., Rodríguez-Fernández, N. J., Zsoter, E., Buontempo, C., & Thépaut, J. N. (2021). ERA5-Land: A state-of-the-art global reanalysis dataset for land applications. *Earth System Science Data*, *13*, 4349–4383. https://doi.org/10.5194/essd-13-4349-2021

Nagler, T., Rott, H., Ripper, E., Bippus, G., & Hetzenecker, M. (2016). Advancements for snowmelt monitoring by means of Sentinel-1 SAR. *Remote Sensing*, *8*. https://doi.org/10.3390/rs8040348

Nefeslioglu, H. A., Sezer, E. A., Gokceoglu, C., & Ayas, Z. (2013). A modified analytical hierarchy process (M-AHP) approach for decision support systems in natural hazard assessments. *Computers and Geosciences*, *59*, 1–8. https://doi.org/10.1016/j.cageo.2013.05.010

Ngo, T. T., & Letchford, C. W. (2009). Experimental study of topographic effects on gust wind speed. *Journal of Wind Engineering and Industrial Aerodynamics*, *97*, 426–438. https://doi.org/10.1016/j.jweia.2009.06.013

Nie, Y., Pritchard, H. D., Liu, Q., Hennig, T., Wang, W., Wang, X., Liu, S., Nepal, S., Samyn, D., Hewitt, K., & Chen, X. (2021). Glacial change and hydrological implications in the Himalaya and Karakoram. *Nature Reviews Earth and Environment*, *2*, 91–106. https://doi.org/10.1038/s43017-020-00124-w

Nolin, A. W., Sproles, E. A., Rupp, D. E., Crumley, R. L., Webb, M. J., Palomaki, R. T., & Mar, E. (2021). New snow metrics for a warming world. *Hydrological Processes*, *35*. https://doi.org/10.1002/hyp.14262

Pomeroy, J. W., Gray, D. M., Shook, K. R., Toth, B., Essery, R. L. H., Pietroniro, A., & Hedstrom, N. (1998). An evaluation of snow accumulation and ablation processes for land surface modelling. *Hydrological Processes*, *12*, 2339–2367.

Pratap, B., Dobhal, D. P., Mehta, M., & Bhambri, R. (2015). Influence of debris cover and altitude on glacier surface melting: A case study on Dokriani Glacier, Central Himalaya, India. *Annals of Glaciology*, *56*, 9–16. https://doi.org/10.3189/2015AoG70A971

Qin, Y., Abatzoglou, J. T., Siebert, S., Huning, L. S., AghaKouchak, A., Mankin, J. S., Hong, C., Tong, D., Davis, S. J., & Mueller, N. D. (2020). Agricultural risks from changing snowmelt. *Nature Climate Change*, *10*, 459–465. https://doi.org/10.1038/s41558-020-0746-8

Rehman, S., Hasan, M. S. U., Rai, A. K., Rahaman, M. H., Avtar, R., & Sajjad, H. (2022a). Integrated approach for spatial flood susceptibility assessment in Bhagirathi sub-basin, India using entropy information theory and geospatial technology. *Risk Analysis*, *2022*, 1–16. https://doi.org/10.1111/risa.13887

Rehman, S., Sajjad, H., Masroor, M., Rahaman, M. H., Roshani, Ahmed, R., & Sahana, M. (2022b). Assessment of evidence-based climate variability in Bhagirathi sub-basin of India: a geostatistical analysis. *Acta Geophysica*, *70*, 445–463. https://doi.org/10.1007/s11600-022-00726-6

Rehman, S., Sayeed, M., Hasan, U., Rai, A. K., Avtar, R., & Sajjad, H. (2021). Assessing flood-induced ecological vulnerability and risk using GIS-based in situ measurements in Bhagirathi sub-basin, India. *Arabian Journal of Geosciences*, *14*. https://doi.org/10.1007/s12517-021-07780-2/Published

Reynolds, D., & Lundquist, J. D. (2019). Evaluating downscaled wind data using snow depth patterns. *AGU Fall Meeting Abstracts*, *2019*, C33B–1571.

Rounce, D. R., Hock, R., & Shean, D. E. (2020). Glacier mass change in High Mountain Asia through 2100 using the open-source Python Glacier Evolution Model (PyGEM). *Frontiers in Earth Science*, *7*. https://doi.org/10.3389/feart.2019.00331

Roy, D. P., Huang, H., Boschetti, L., Giglio, L., Yan, L., Zhang, H. H., & Li, Z. (2019). Landsat-8 and Sentinel-2 burned area mapping - A combined sensor multi-temporal change detection approach. *Remote Sensing of Environment*, *231*. https://doi.org/10.1016/j.rse.2019.111254

Saaty, T. L. (1990). How to make a decision - The Analytic Hierarchy Process. *European Journal of Operational Research*, *48*, 9–26.

Schmidt, R. A. (1980). Threshold wind speeds and elastic impact in snow transport. *Journal of Glaciology*, *26*, 453–467.

Schweizer, J., Jamieson, J. B., & Schneebeli, M. (2003). Snow avalanche formation. *Reviews of Geophysics*, *41*. https://doi.org/10.1029/2002RG000123

Singh, A., & Ganju, A. (2002). Earthquakes and avalanches in Western Himalaya. *Proceedings of the 12th symposium on earthquake engineering*, 18.

Singh, D. K., Mishra, V. D., & Gusain, H. S. (2020). Simulation and analysis of a snow avalanche accident in Lower Western Himalaya, India. *Journal of the Indian Society of Remote Sensing*, *48*, 1555–1565. https://doi.org/10.1007/s12524-020-01178-5

Singh, M. K., Thayyen, R. J., & Jain, S. K. (2021). Snow cover change assessment in the upper Bhagirathi basin using an enhanced cloud removal algorithm. *Geocarto International*, *36*, 2279–2302. https://doi.org/10.1080/10106049.2019.1704069

Smith, T., & Bookhagen, B. (2018). Changes in seasonal snow water equivalent distribution in High Mountain Asia (1987 to 2009). *Science Advances*, *4*. https://doi.org/10.1126/sciadv.1701550

Smith, T., & Bookhagen, B. (2020). Assessing multi-temporal snow-volume trends in High Mountain Asia from 1987 to 2016 using high-resolution passive microwave data. *Frontiers in Earth Science*, *8*. https://doi.org/10.3389/feart.2020.559175

Snehmani, Bhardwaj, A., Pandit, A., & Ganju, A. (2014). Demarcation of potential avalanche sites using remote sensing and ground observations: A case study of Gangotri glacier. *Geocarto International*, *29*, 520–535. https://doi.org/10.1080/10106049.2013.807304

Stigter, E. E., Litt, M., Steiner, J. F., Bonekamp, P. N., Shea, J. M., Bierkens, M. F., & Immerzeel, W. W. (2018). The importance of snow sublimation on a Himalayan glacier. *Frontiers in Earth Science*, *6*. https://doi.org/10.3389/feart.2018.00108

Strasser, U., Bernhardt, M., Weber, M., Liston, G. E., & Mauser, W. (2008). Is snow sublimation important in the alpine water balance? *The Cryosphere*, *2*, 53–66. www.the-cryosphere.net/2/53/2008/

Teich, M., Bartelt, P., Grêt-Regamey, A., & Bebi, P. (2012). Snow avalanches in forested terrain: Influence of forest parameters, topography, and avalanche characteristics on runout distance. *Arctic, Antarctic, and Alpine Research*, *44*, 509–519. https://doi.org/10.1657/1938-4246-44.4.509

Terink, W., Lutz, A. F., Simons, G. W., Immerzeel, W. W., & Droogers, P. (2015). SPHY v2.0: Spatial Processes in HYdrology. *Geoscientific Model Development*, *8*, 2009–2034. https://doi.org/10.5194/gmd-8-2009-2015

Thayyen, R. J., Gergan, J. T., & Dobhal, D. P. (2007). Role of glaciers and snow cover on headwater river hydrology in monsoon regime - Micro-scale study of Din Gad catchment. *Current Science*, *92*, 376–382. https://www.jstor.org/stable/24096736

UDM 2 [Accessed on November 3, 2022]. (2022). Planet Labs PBC. https://developers.planet.com/docs/data/udm-2/

van Rossum, G. (2023). *The Python language reference*. Python Software Foundation. https://docs.python.org/3/reference/index.html

Viviroli, D., Dürr, H. H., Messerli, B., Meybeck, M., & Weingartner, R. (2007). Mountains of the world, water towers for humanity: Typology, mapping, and global significance. *Water Resources Research*, *43*. https://doi.org/10.1029/2006WR005653

Wagenbrenner, N. S., Forthofer, J. M., Lamb, B. K., Shannon, K. S., & Butler, B. W. (2016). Downscaling surface wind predictions from numerical weather prediction models in complex terrain with WindNinja. *Atmospheric Chemistry and Physics*, *16*, 5229–5241. https://doi.org/10.5194/acp-16-5229-2016

Wayand, N. E., Marsh, C. B., Shea, J. M., & Pomeroy, J. W. (2018). Globally scalable alpine snow metrics. *Remote Sensing of Environment*, *213*, 61–72. https://doi.org/10.1016/j.rse.2018.05.012

Winstral, A., Elder, K., & Davis, R. E. (2002). Spatial snow modeling of wind-redistributed snow using terrain-based parameters. *Journal of Hydrometeorology*, *3*, 524–538.

Yadav, J. S., Misra, A., Dobhal, D. P., Yadav, R. B., & Upadhyay, R. (2021). Snow cover mapping, topographic controls and integration of meteorological data sets in Din-Gad basin, Central Himalaya. *Quaternary International*, *575-576*, 160–177. https://doi.org/10.1016/j.quaint.2020.05.030

Zhang, H., Immerzeel, W. W., Zhang, F., de Kok, R. J., Chen, D., & Yan, W. (2022). Snow cover persistence reverses the altitudinal patterns of warming above and below 5000 m on the Tibetan Plateau. *Science of the Total Environment*, *803*. https://doi.org/10.1016/j.scitotenv.2021.149889